RICE UNIVERSITY

Systems for the Radiative Trapping of Lithium and the Tuning of its Interactions via Magnetic Field Control

by

Christopher John Welford

A Thesis Submitted
in Partial Fulfillment of the
Requirements for the Degree

Master of Science

Approved, Thesis Committee:

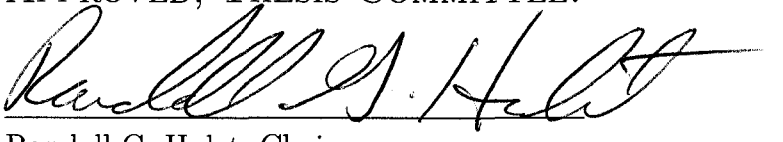

Randall G. Hulet, Chairman
Fayez Sarofim Professor of Physics and
Astronomy

Thomas C. Killian
Associate Professor of Physics and
Astronomy

Christopher Johns-Krull
Assistant Professor of Physics and
Astronomy

Houston, Texas

October 2007

UMI Number: 1455297

INFORMATION TO USERS

The quality of this reproduction is dependent upon the quality of the copy submitted. Broken or indistinct print, colored or poor quality illustrations and photographs, print bleed-through, substandard margins, and improper alignment can adversely affect reproduction.

In the unlikely event that the author did not send a complete manuscript and there are missing pages, these will be noted. Also, if unauthorized copyright material had to be removed, a note will indicate the deletion.

UMI®

UMI Microform 1455297

Copyright 2008 by ProQuest LLC.

All rights reserved. This microform edition is protected against unauthorized copying under Title 17, United States Code.

ProQuest LLC
789 E. Eisenhower Parkway
PO Box 1346
Ann Arbor, MI 48106-1346

ABSTRACT

Systems for the Radiative Trapping of Lithium and the Tuning of its Interactions via Magnetic Field Control

by

Christopher John Welford

An all diode laser system has been constructed for the confinement of ^{7}Li in a magneto-optical trap (MOT), which is the first stage in a Bose-Einstein condensate (BEC) experiment. The system is based around an anti-reflection coated broad-area laser which provides the MOT power. The system allows the production of a MOT containing 1.6×10^{10} atoms at 600 μK and densities in excess of 2×10^{11} atoms/cm^3. In addition, a magnetic field control system has been implemented using feedback from an Ultrastab 866 current sensor. The system provides a fractional current stability of 1 part in 10^4 - a factor of four improvement over the previous scheme where the current limit of the supply was relied upon for stability.

Contents

Abstract i

List of Figures iv

1 Introduction **1**

2 The Diode Laser Systems **3**

2.1 Introduction 3

2.2 The ^{7}Li Laser System 5

2.3 The ^{6}Li Laser System 15

2.4 The Future of the Diode Laser Systems 18

3 Field Stabilization and Control **20**

3.1 The Use of Magnetic Fields to Tune Atomic Interaction 20

3.2 The Old Scheme 21

3.3 The Ultrastab 866 Current Sensor (The "Danfysik") 24

3.4 The Feedback Circuit 24

3.5 The Control Scheme 26

3.6 The New Sequence 32

3.7 Ramping Performance 34

3.8 Stabilization 35

3.9 Summary and Future Work 43

Appendices **20**

A MOSFETs **47**

A.1 A Brief Introduction to MOSFETs 47

A.2 MOSFETs and the feedback system 48

B The Switch Box 51

References 53

List of Figures

1.1 The Apparatus 2

2.1 The Energy Levels of the ^{7}Li MOT 4
2.2 The ^{7}Li Laser System 6
2.3 The Timing Sequence for the Cooling and Compression of the MOT . 11
2.4 Cross-sections of the ^{7}Li MOT Before and After Cooling and Compression 13
2.5 Time of Flight Expansion of the ^{7}Li MOT Before and After Cooling and Compression 14
2.6 ^{7}Li MOT Parameters Before and After the Cooling and Compression 14
2.7 The ^{6}Li Laser System 16

3.1 Scattering length vs field the F = 1, $m_F = 1$ state of ^{7}Li 21
3.2 The Previous Sequence 22
3.3 The Old High-Field Ramp 23
3.4 The Feedback Circuit 25
3.5 The system layout 27
3.6 Digital/analog control switching circuit 28
3.7 The floating buffers 30
3.8 The supply limit control circuit 31
3.9 The Timing Sequence. 32
3.10 The IntuiLink software interface 34
3.11 Field Ramp Art 35
3.12 Ramping the Field Using the Feedback System 35
3.13 The Zeeman sublevels of the 2 $^2S_{\frac{1}{2}}$ level of ^{7}Li 36
3.14 RF resonances for the F = 1, $m_F = 1$ to F = 2, $m_F = 2$ transition of ^{7}Li 37
3.15 The Noise and Repeatability of the Agilent 33220A Arb. 39

3.16 The Long Term Noise/Drift of the Home Made Ramp Circuit 40
3.17 An RF Resonance Using a Home Made Ramp Circuit 41
3.18 The Noise Spectrum of the Feedback Stabilized Field 42

A.1 MOSFET Circuit Symbols 48
A.2 MOSFET Construction 49
A.3 Drain Current vs Gate-Source Voltage 50

B.1 The Switch Box 52

Chapter 1
Introduction

Since I joined the Hulet lab there have been two cold-atom apparatuses in the lab - the older EMT1 (Electro-Magnetic Trap 1) with lead students Kevin Strecker and Guthrie Partridge, and the newer EMT2 (see Fig. 1.1) on which I work with fellow grad students Mark Junker, Dan Dries, and James Hitchcock. EMT1 has been very successful. It was the first apparatus to produce a degenerate Fermi gas of lithium [1], and has produced studies of bright matter wave solitons in a Bose-Einstein condensate (BEC) [2], long lived bosonic molecules of fermionic ^{6}Li [3], and more recently pairing of ^{6}Li in the BEC-BCS (Bardeen-Cooper-Shrieffer) crossover regime [4].

Due to this success and technology developed along the way, the newer EMT2 apparatus was based on EMT1 and broadly speaking follows the same experimental procedure. Atoms are initially loaded in a magneto-optical trap before transfer to a magnetic trap. RF evaporation in the magnetic trap cools the atoms which are transferred to an optical dipole trap formed by a focused 1030 nm laser. EMT2 is not a clone of EMT1, however. New technologies and hindsight courtesy of previous students has allowed us to make changes to the way various parts of the experiment are performed to improve performance, reliability and ease of use.

This thesis documents two of my contributions to the apparatus. The first is a diode laser system for trapping ^{7}Li in a MOT. The system is much smaller than the previous dye laser solutions due to the inherently small footprint of diode lasers, and more modular since as it is composed of multiple lower power lasers. Acousto-optic modulators (AOMs) are used to control the output of the system allowing the output frequencies to be changed quickly and independently in a way not possible with previous laser systems in our lab.

The second improvement is the implementation of an easy to program control

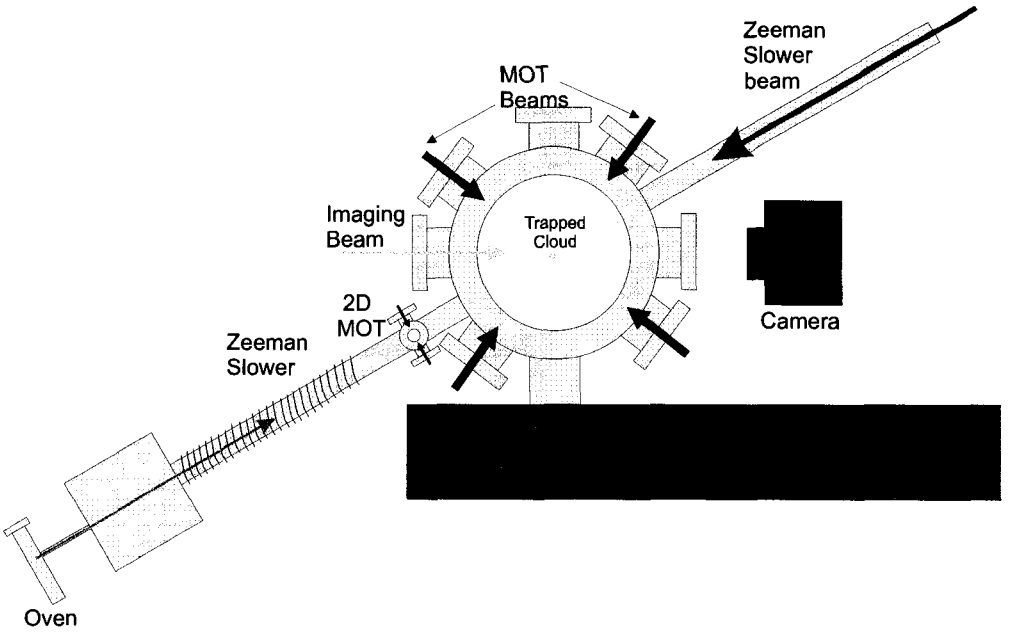

Figure 1.1 A cartoon showing the configuration of the apparatus.

system for changing the current in the bias coils of our apparatus. These coils are energized during the optical trap stage of our experiments and are responsible for controlling the sign and strength of atom-atom interactions. The system uses active feedback to control the current allowing for fast field ramps without waiting for the power supplies to respond or relying on their innate stability.

Chapter 2
The Diode Laser Systems

2.1 Introduction

Originally, the main laser from which the trapping and probing light for EMT2 was derived was produced from a single Spectra Physics 380D dye laser shared with EMT1 [5]. In order to separate the two experiments so they could operate simultaneously, it was necessary to construct a new laser system. The laser system was required to match and ideally exceed the $\approx$ 30 mW usable MOT power from the 380D and provide an additional 50 mW for Zeeman slowing of the atoms. Stability/linewidth small compared to the detuning from resonance of 40 MHz was needed for stable loading of the MOT (straightforward given the $\sim$1 MHz linewidths readily achievable with external cavity diode lasers [6]).

Fig. 2.1 shows the transitions used for operation of the ^{7}Li MOT. The laser system would have to produce light $\approx$ 40 MHz negative (or red) detuned from both transitions to produce a trapping force, as well as light detuned $\approx$ 1 GHz red of the cycling transition for the Zeeman slower (which cools the atoms so that a significant number are within the velocity capture range of the MOT). Atoms are trapped and nominally cycle on the $2\ ^2S_{1/2}\ F = 2 \leftrightarrow 2\ ^2P_{3/2}\ F = 3$ transition but are frequently driven to the $2\ ^2P_{3/2}\ F = 2$ level by off-resonant excitation. They may then either decay to the $2\ ^2S_{1/2}\ F = 2$ level at which point cycling continues, or the $2\ ^2S_{1/2}\ F = 1$ level where they fall out of resonance with with the cycling light and are lost. The addition of a repump containing 30% of the total optical power in the MOT ensures atoms that decay to this state are re-excited and make their way back onto the cycling transition.

Historically speaking, using diode lasers to trap lithium has been difficult due to an absence of high power, single-longitudinal mode lasers at 671 nm. In previous years

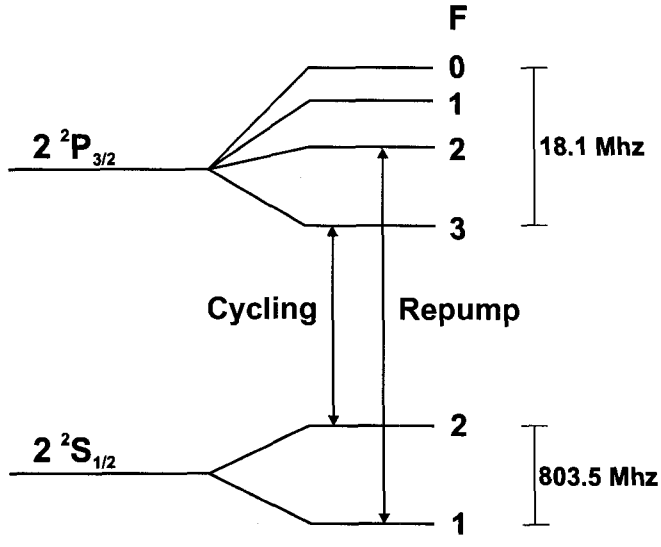

Figure 2.1 The energy levels of the D2 line of ^{7}Li showing the transitions used for MOT operation. F is the total angular momentum of the atom including the nuclear spin, I and the electronic angular momentum, J. The 2F+1 fold degeneracy of the F levels enforces the asymmetric energy splitting shown in the diagram.

the only devices capable of producing sufficient power have been tapered amplifier devices from a company called SDL. These have since gone out of production, making the use of these devices as the basis for a laser system unwise due to the lack of replacements. Fortunately, John Gaebler [7] had some success in getting ~60 mW in a reasonable mode from a High Power Devices (HPD) model HPD1310 670nm Broad Area Laser (BAL). These devices naturally have poor mode structure, but this device was sent to Sacher-Lasertechnik to be coated with an anti-reflective coating to reduce the reflectivity of the output facet and suppress the natural lasing modes. After coating it was possible to inject [6] (force the "slave" to lase at the same frequency, and with the same linewidth and phase, as the "master") the device in a similar manner to a normal diode, bringing only a single mode above the lasing threshold. That mode has far more power than that characteristic of an un-coated device, though the overall power of the device is reduced.

We decided to use this device and one of the remaining tapered amplifier devices

(SDL7630-E S/N:233) as the basis for an independent ^{7}Li laser system - the BAL providing the MOT light, and the tapered amplifier the Zeeman slower light. The system was designed to be able to change the light intensity and frequency so as to reproduce the cooling and compression sequences documented in Ref. [8]. The slaves were seeded using beams double passed through AOMs such that their pointing changed (relatively) little as the frequency was varied. Thus the slave laser frequency would be tunable by sweeping the AOM drive frequency with no consequence to the pointing of the slaves which needed to be stable in order to seed the BAL and tapered amplifier.

2.2 The ^{7}Li Laser System

Fig. 2.2 shows the layout of the ^{7}Li laser system. The majority of the system including all the diodes are mounted on a 4 ft by 2 ft damped optics breadboard which is isolated from vibrations on the main optics table by damping rubber.

The first element of the system - the master - is a Bluesky Research Circulaser diode (P/N: PS110-00) designed for 658 nm. Bluesky tests the actual wavelength of their diodes allowing us to request diodes closer to our needed wavelength. Thus in practice the wavelength of the diode is 661 nm, 10 nm from our needed wavelength of 671nm. The diode can be tuned the remaining way using an external cavity (the diode is in Littrow configuration [6, 9]) and by heating the diode. In the case of this device we run the diode at 45 °C where it outputs ~30 mW at its operating current, down 20 mW from its rated 50 mW. Heating diodes has a detrimental effect on the lifetime of the device, but the effect does not seem too severe since at the time of writing this laser has been in use for 3 years.

The master is side-locked to a Fabry-Perot cavity which provides feedback to reduce frequency noise. This cavity is in turn locked to the D2 line ($2^2S_{1/2}$ F = 2 $\leftrightarrow$ $2^2P_{3/2}$ F = 3 transition) of ^{7}Li via a saturated absorption lock [10], which provides

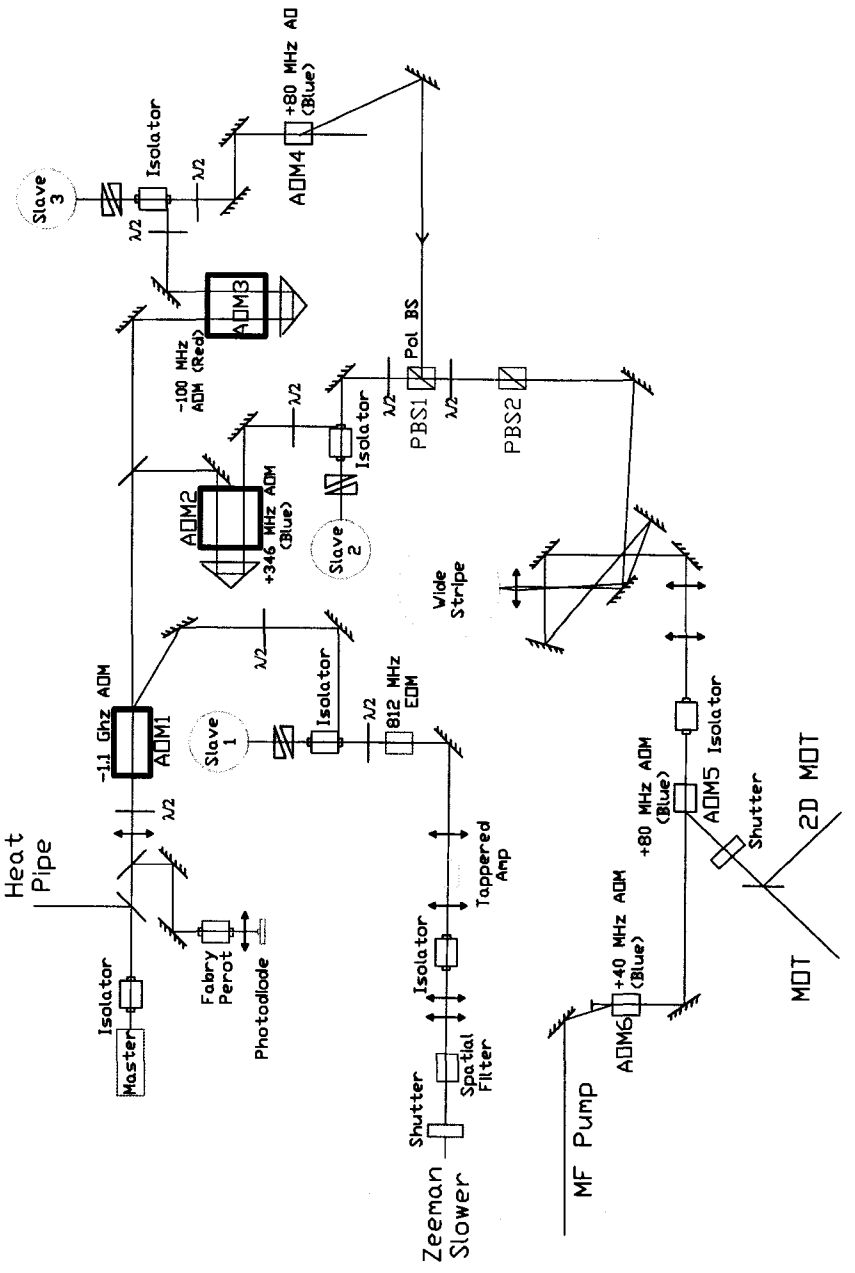

Figure 2.2 The ^{7}Li laser system.

an absolute frequency reference to prevent drifting. Light from this laser is used to provide the seeding light for lasers on the cycling transition, repump transition and the Zeeman slower.

A double-passed Intraaction ATD901A1 acouso-optic deflector (AOM3 in Fig. 2.2) detunes some of the master laser light -200 MHz from resonance with the cycling transition before seeding a Mitsubishi ML101J8 45 mW diode purchased from Thorlabs (slave 3). These lasers have a center design wavelength of 660 nm but can be wavelength selected for 664 nm which is sufficiently close to pull them with injection to 671 nm if heated to 50 °C (at which point they output ~30 mW). The output of the diode passes through an Intraaction ATM-80A1 AOM (AOM4) at +80 MHz (bringing the overall detuning to -120 MHz with respect to the cycling transition) before seeding the BAL. AOM4 allows the intensity of the cycling light to be lowered independently of the repump light by lowering the fraction of cycling light seeding the BAL.

Light detuned -120 MHz from the repump transition is produced by shifting the light from the master laser +692 MHz using a double-passed Intraaction ATM3001A1 AOM (AOM2) at 346 MHz. The light is used to seed a 20 mW RLT6720MG diode laser (slave 2), which is mixed with the output of slave 3 before seeding the BAL.

The beams are overlapped and mixed together using a pair of polarizing beam-splitting cubes (PBS1 and PBS2) and a $\lambda/2$ wave-plate. The orthogonally polarized beams are overlapped spatially at PBS1, after which a wave-plate rotates the polarizations of the components of the overlapped beams such that both frequency components have projections in the plane of the table, which are transmitted by PBS2. Adjustment of the angle of the wave-plate allows the power ratio of the two frequencies to be adjusted to peak up the loading of the MOT.

The optical setup for seeding the BAL and picking off the seeded mode is described in references [7, 11], and shown in Fig. 2.2. The output of the BAL is highly astig-

matic, divergent and contains significant amounts of amplified spontaneous emission (ASE). After passing through the cylindrical lens nearest the laser, the vertical and horizontal axes (which are diverging at different rates) are collimated by two cylindrical lenses. The focal lengths of the lenses are chosen so as to make the seeded mode roughly circular in shape so it can be filtered to remove ASE and produce a roughly TEM00 mode. Obtaining some seeded power from the BAL is fairly straight forward with only the vertical being highly sensitive. However, obtaining higher powers from the device and producing good fiber coupling requires a significant amount of time be spent finding a good mode, peaking the power up, and beam-shaping. The power is best optimized after beam-shaping, where the modes can be isolated from each other and the ASE using a pinhole and the useful power quantitatively measured.

The BAL is protected from back reflections by a Gsänger optical isolator which provides $\geq$40 dBm of isolation. Optical isolators are present on the outputs of all the lasers as the susceptibility to light with makes injection locking possible also makes them highly sensitive to stray laser light within a few nanometers, particularly from themselves (optical feedback) and the other lasers in the system. After the isolator the light passes through a NEOS Technologies 23080-1 AOM (AOM5) which shifts both the cycling and repump light +80 MHz towards resonance to their final values $\approx$ -40 MHz from their respective transitions.

The MOT light is fiber-coupled (which filters ASE and ensures only the power in a TEM_{00} mode is transmitted) to the apparatus table. A photodiode after the fiber can be used to peak up the alignment of the BAL, but this is difficult due to thermal hysteresis in the BAL and the coupling of the alignment of the fiber and seeding. As such it is best to restrict adjustments after the fiber to the vertical alignment of the seeding which does not change the pointing of the BAL output, and the alignment of the fiber. The pointing of the BAL is temperature sensitive, and sometimes shifts until fully warmed up, requiring small adjustments to the fiber coupling.

The Zeeman slower light is produced by shifting the light from the master ~1.1 GHz red using a 1.1 GHz Brimrose AOM (AOM1). It seeds a ML101J8 laser which is passed through a 812 MHz electro-optic modulator (to produce sidebands, one of which is at the repump frequency to provide repumping for the Zeeman slower) before in turn seeding the tapered amplifier [12]. The tapered amplifier is beam-shaped, isolated (using an Isowave I67T5H isolator) and collimated using a microscope objective, before being *free space* coupled (simply shot over the gap between the two tables) to the apparatus table.

M_F optical pumping is a process in which all the atoms in the MOT (which does not select between Zeeman sub-levels) are transferred to a single state, in our case the F = 2, M_F = 2 state. It is necessary because only low field seeking states are magnetically trap-able, and multiple spin states results in spin decay. If the MOT was simply transferred directly to the magnetic trap with no M_F pumping, initial loading would only be 40%, and would be followed by huge spin decay losses due to spin exchange collisions between pairs of F = 2, M_F = 1 atoms, and F = 2, M_F = 1 and F = 2, M_F = 2 atoms. It requires as much power as possible (to ensure efficient pumping at far detuning), as far detuned as possible (to ensure the entire, optically-dense cloud is pumped). In our case we use the zeroth-order of AOM5 which contains both cycling and repump light, detuned -120 MHz from their respective transitions. The light is passed through a 40 MHz Intraaction AOM-40 (AOM6) which acts as both a fast switch as well as shifting the frequency. At regular MOT detunings this would produce light at -80 MHz but for the duration of the M_F pumping we sweep AOM2 and AOM3 as far as they will go while keeping Slave 1 and Slave 2 injection locked so that we M_F pump at -105 MHz. The light is fiber coupled to improve beam quality and improve pointing stability. Since the first order of AOM5 produces the MOT beam which is turned off during M_F pumping, the M_F pump receives the full power of the BAL resulting in a ~45 mW of M_F pump light after the fiber.

To prevent leakage light from the AOMs impacting the lifetime of the magnetic trap, there are mechanical shutters in the paths of the MOT and Zeeman slower beams allowing the light to be blocked. The MOT shutter is positioned after AOM5 such that it serves to also block the M_F pump. In addition to these (relatively) slow shutters, the MOT also has a fast ($\leq$1 ms) shutter to ensure leakage from the MOT is removed as quickly as possible, since the MOT remains on until on a few milliseconds before the magnetic trap. The Zeeman slower can be turned off much earlier (before the cooling and compression), and a slow shutter is sufficient. In addition to the shutters, the path between the laser table and apparatus table is blocked by curtains and beam-blocks, other than where absolutely necessary, to prevent stray light entering the chamber.

The current for the master laser is supplied by a home made current controller based on references [13, 14]. The current for the slave lasers is supplied by an ILX LDC-3916370 controller which also provides temperature control for all the diode lasers. In addition to the ILX 3916372 500 mA modules which drive the slaves the controller has a single 3916376 mA 1.5 A module used to supply the current for the BAL (1.4 A). Current for the tapered amplifier is supplied by a ILX Lightwave LDX-3545 controller.

The frequency of light of both the cycling and repump can be varied independently by use of the double-pass AOMs/AODs which produce the seeding beams for the slaves that seed the BAL *without* affecting their intensities. This is in contrast to the dye laser systems used in our lab to trap ^{7}Li [5, 8], where the cycling and repump are coupled by an EOMs, and the only way to change the frequencies relative to each other is to change the EOM drive frequency (which also changes the relative intensities). Another side effect of the EOMs is they put a significant amount of power in an unused sideband effectively *dumping* around 25% of the optical power. As a result the diode system is more flexible and efficient.

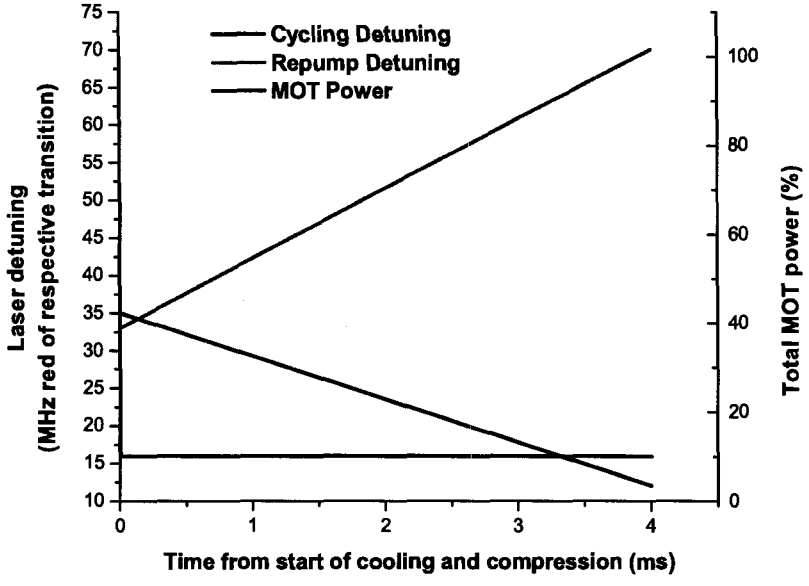

Figure 2.3 The timing sequence for the cooling and compression of the MOT, showing the frequency sweeps for the cycling and repump light, and how the total optical power is varied.

Cooling and compression is a process used to raise the density and lower the temperature of the MOT prior to transfer to the magnetic trap. It represents the first of several cooling stages throughout the experiment and improves loading of the magnetic trap. The cooling and compression must be performed in a short period of time before transfer to the magnetic trap, as the conditions which optimize the cooling and compression significantly reduce the load rate of the MOT, and lead to a large decrease in the steady-state number. We use a cooling and compression sequence similar to that used in Ref. [15], and a timing diagram of is shown in Fig. 2.3.

The cycling and repump lasers are initially at -35 MHz and -33 MHz relative to their respective transitions, where the MOT load rate is experimentally determined to maximize. The cycling detuning is swept closer to resonance to increase density and reduce the temperature, which is given by Eqn. 2.1 (where $\Gamma = 5.9$ MHz is the

linewidth, k_B is the Boltzmann constant, I is the intensity, $I_S = 5.1mW/cm^2$ is the saturation intensity and Δ is the detuning).

$$T = \frac{\hbar\Gamma}{4k_B}\frac{1 + 2I/I_S + (2\Delta/\Gamma)^2}{2|\Delta|/\Gamma} \tag{2.1}$$

Experimentally the optimal final value for the cycling frequency has been determined to be -12 MHz for our system. This differs from the value of -3 MHz which minimizes Eqn. 2.1 and gives the doppler limit. Physically, the doppler limit is the temperature associated with the brownian motion of the atoms as they random walk due to the many random kicks they receive as they scatter photons. Unfortunately, since the MOT traps multiple M_F states and has a spatially varying magnetic field, the frequency which minimizes the temperature for an atom in a given M_F in one location is non optimal for an atom in another part of the cloud. Additional M_F states complicate matters further, as does the fact that the cloud becomes optically thick as the detuning decreases, limiting the ability for photons to actually penetrate the cloud and cool atoms effectively. The value of -12 MHz we observe is therefore the value which balances these factors to give the best results for our conditions.

In contrast to the frequency of the cycling light, the repump detuning is swept away from resonance, and the atoms now scatter cycling photons far more preferentially than repump photons since the scattering rate is proportional to:

$$\frac{2I/I_S}{1 + 2I/I_S + (2\Delta/\Gamma)^2} \tag{2.2}$$

The 2 $^2S_{\frac{1}{2}}$ F = 1 state thus acts as a psuedo dark-state where density-limiting reradiation effects (photons emitted from one atom are immediately absorbed by a neighboring atom, creating an effective repulsion) are minimized. The power in both cycling and repump is reduced to 10% of the initial value of $\approx 4\ I/I_S$ to compensate for the reduced detuning of the cycling light and further lower the temperature. Fig. 2.4 shows time of flight images of the cooled and compressed MOT taken with fluorescence imaging immediately after turning off the field. By taking series of such

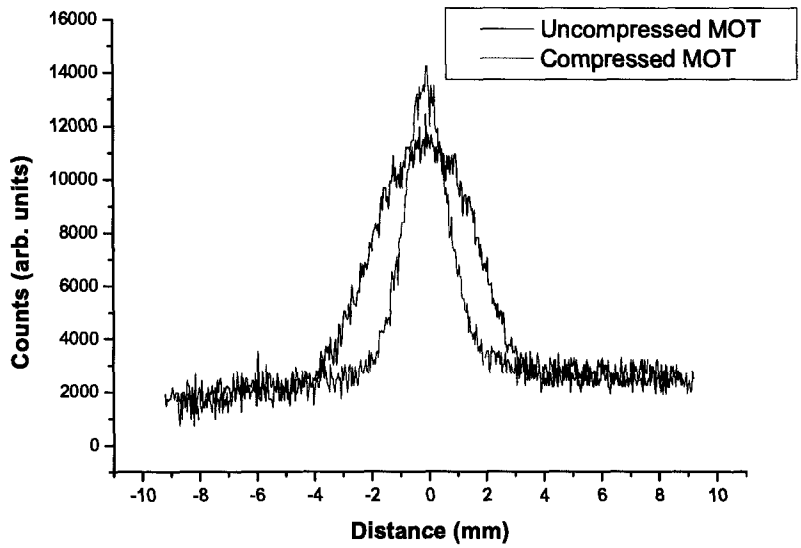

Figure 2.4 Cross-sections of the ^{7}Li MOT before and after the cooling and compression. Images were taken with fluorescence imaging immediately after turning off the MOT field with a 0.1 ms time of flight.

shots at different times after turning off the trap, it was possible to track the (1/e guassian) waist of the MOT as a function of time to measure the temperature. Fig. 2.5 shows data for the axial waist of the MOT for both the steady state case and cooled and compressed case. The fits shown result from fitting the data in Origin to Eqn. 2.3 [16]

$$\omega(t) = \omega_0 \sqrt{1 + \frac{2k_B T t^2}{m\omega^2}} \tag{2.3}$$

where ω is the waist, T is the temperature, t is the time after release, and m is the atomic mass of ^{7}Li.

Fig. 2.6 compares the number, density and temperature of the steady state, and cooled and compressed MOTs. The density is more than doubled and the temperature reduced 20%, at the cost of 20 % number.

Before transfer to the magnetic trap the MOT field and light is turned off and the M_F pump pulsed on for 500 μs in order to ensure the number of atoms in the F = 2, M_F = 2 state is maximized.

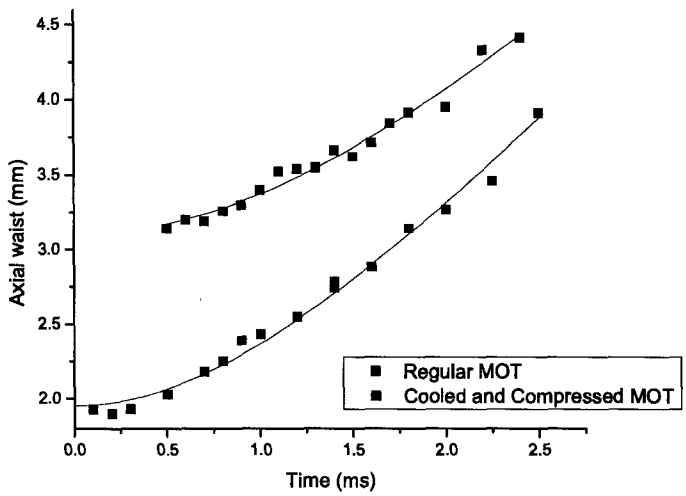

Figure 2.5 The axial waist of the ^{7}Li MOT as a function of time after turning off the MOT field. The red curve is before cooling and compression. The blue curve is after cooling and compression.

	Uncompressed MOT	Compressed MOT
Number, N	2.0×10^{10}	1.6×10^{10}
Density, ρ (atoms/cm^3)	1.08×10^{11}	2.28×10^{11}
Temp. T (mK)	0.73	0.59

Figure 2.6 ^{7}Li MOT parameters before and after the cooling and compression.

2.3 The ^{6}Li Laser System

One of the most attractive qualities of lithium as an element for atom trapping is it has both fermi and bosonic isotopes available. With this in mind we are constructing a new diode system for trapping ^{6}Li in addition to ^{7}Li. ^{6}Li is already in use on EMT1 and the new system has been designed to use the same transitions. Cycling is done on the 2 $^2S_1/2$ F = 3/2 to 2 $^2P_3/2$ F = 5/2 transition, and repumping is done on 2 $^2S_1/2$ F = 1/2 to 2 $^2P_1/2$ F = 3/2 transition. The laser system must be capable of producing light red detuned $\approx$ 40 MHz with the ability to sweep $\pm$30 MHz for cooling and compression. It must be capable of producing $\approx$ 40 mW of total trapping power with 2/3 for the cycling tranistion and 1/3 for the repump. In addition, the system must provide light red detuned $\approx$ 1.1 GHz red detuned of the cycling transition for the Zeeman slower. A single higher power $\geq$30 mW laser diode with no repump has proved adequate for this purpose on EMT1 [17].

Fig. 2.7 shows the current design for the ^{6}Li laser system. While similar to the ^{7}Li system, the spacing of the cycling and repump is too large ($\sim$10 GHz) for a single diode to provide all the frequencies since repumping is done on the D1 line to prevent cross-talk between the ^{6}Li MOT and ^{7}Li MOT as discussed in Ref. [17]. A single ML101J8 master laser, ECDL1, is side-locked to a cavity followed by a saturated absorption lock in a heat-pipe cell on resonance with the cycling transition. It seeds a single slave (slave1) after the double-pass deflector AOM7 (deflectors have proved to give superior scan range from our experiences with the ^{7}Li) with additional master lasers (ECDL1 and ECDL2) frequency-offset locked to the first to provide light at the correct detunings for the repump and Zeeman slower. The "offset locks" are described in Ref. [18] and require power to be split from both ECDL1 and ECDL2 to produce beatnotes between them and ECDL1 on a pair of photodiodes (10 GHz in the case of the repump and 1 GHz for the Zeeman slower) which are processed to produce error signals which are used to control their relative frequencies.

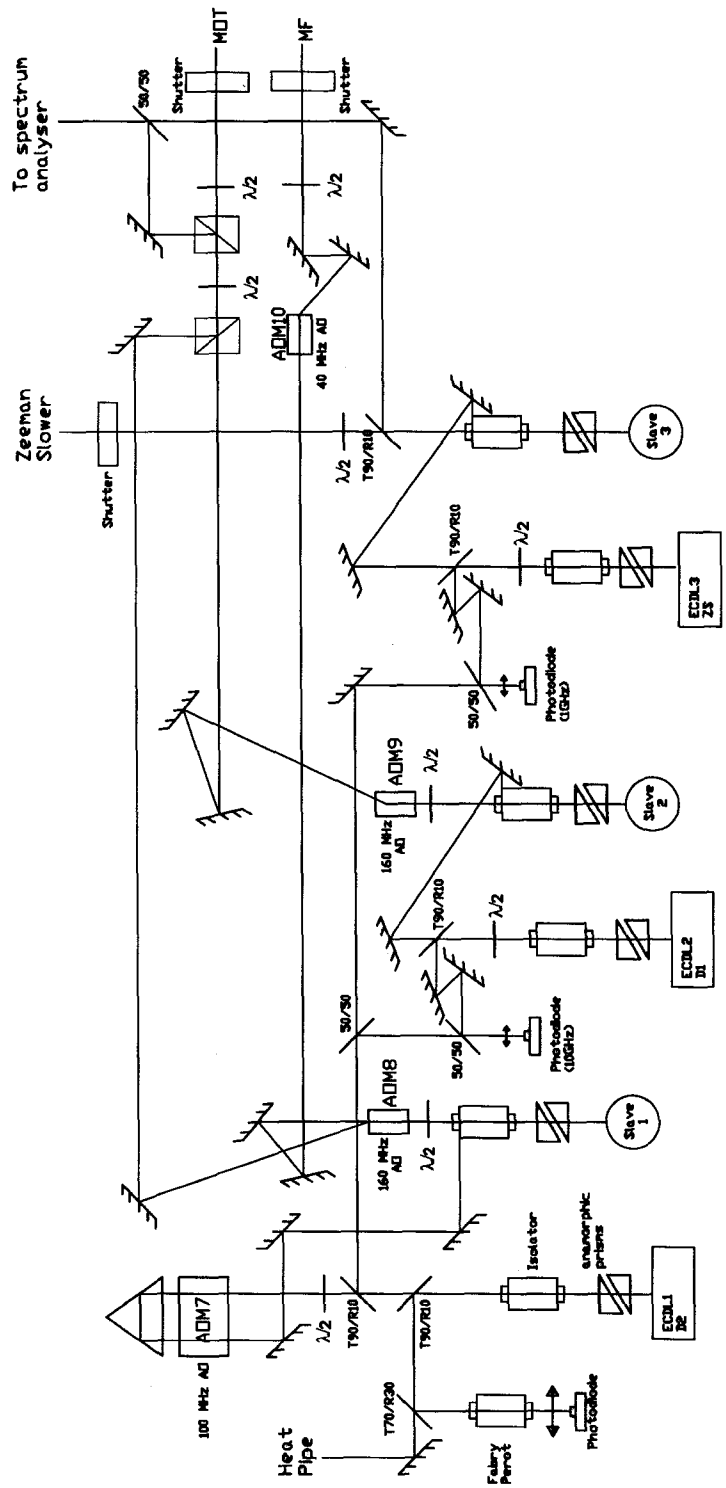

Figure 2.7 The ^{6}Li laser system.

Light from external cavity diode laser (ECDL) 1 is double passed -200 MHz through AOM7, then brought back +160 MHz by AOM8 to produce light -40 MHz off resonant with the cycling transition. This seeds a HL6555G diode (slave1) which produces the MOT cycling light. The HL6555G diodes are manufactured by Hitatchi/OPnext and are rated to output 70 mW at 664 nm. Our experiences with our current batch have been very positive, obtaining close to their rated maximum power in slave configuration even after heating to $35 - 40\,^{\circ}\mathrm{C}$ to allow the device to lock up at 671 nm. These diodes also work well in master lasers where they output 55 mW. These diodes are currently the most powerful (well behaved) diodes we have used.

The repump master, ECDL2 (again an ML101J8), is frequency-locked such that the HL6555G slave it seeds (slave2) is -40 MHz detuned from the repump after passing through AOM9 at 160 MHz. The Zeeman slower master, ECDL3, is frequency locked 1.1 GHz red using an offset lock and used to seed a HL6555G diode (slave3) which provides ≈60 mW of Zeeman slower power.

The cycling and repump light are mixed and *free space* coupled to the apparatus table to be mixed with the ^{7}Li light to produce a dual MOT. We anticipate the system will produce 45-50 mW of MOT power. M_F pumping for the ^{6}Li is derived from the unshifted order of AOM8 passed through AOM10 at 40 MHz so that it contains all the power of slave1 (ignoring power loss due to the AOMs) tunable anywhere from ≈ -120 MHz to -280 MHz as proves needed. The repump light will be pulsed on in MOT configuration during M_F pumping to prevent pumping to a dark state. The total power available for M_F pumping should be ≈ 60 mW including both frequencies.

As with the ^{7}Li system, all lasers are protected by optical isolators (OFR model IO-3-671-LP for masters and IO-3-671-LP/PBS for slaves).

2.4 The Future of the Diode Laser Systems

Currently light used for imaging for the ^{7}Li is derived from the zeroth order of AOM4 which is otherwise unused and has the full power of ^{7}Li slave 3 for imaging. Additional power is taken from light rejected from PBS2, and both of these beams are shifted with AOMs producing the frequencies needed to probe the F = 1, M_F = 1 state in the low and high fields and the F = 2, M_F = 2 states in the low field. While this works reasonably well, AOMs have a finite tuning range of ≈50% of their nominal value (twice if double passed), leading to gaps in the range of fields that can be probed and requiring four AOMs to produce all the frequencies. Moreover the optics and electronics needed for this system take up a significant amount of the limited space available on our optics table.

We have constructed an additional master laser for dedicated imaging which is frequency offset locked with respect to slave 2 of the ^{7}Li system using a "SOFT" lock [19, 20]. By tuning a VCO in the lock the probe laser can be scanned from 500-1700 MHz red of slave 2 to which it is locked. This new laser has been implemented into the ^{7}Li setup and is being tested. It allows the imaging of the F = 1, M_F = 1 state from 490 G and up through the high field as well as the F = 2, M_F = 2 state in the low field. Since the pointing of the laser does not change as the lock is scanned no realignment of the AOM used to switch the probe on and off is required. The large tuning range of the lock removes the "blind-spots" inherent to the multiple AOM solution. Additionally, the laser and most of the optics for this system fits on the 8'×4' optics table housing the rest of the laser system, freeing up several square feet of space on the main optics table.

Recently the tapered amplifier used as the Zeeman slower died and had to be replaced. We have replaced it with 70 mW HL6555G diode as in the ^{6}Li setup. While the diode outputs less total power than the tapered amplifier, the useful power at the apparatus table is similar in both cases and performance appears to be comparable.

The BAL used for the ^{7}Li laser system currently has no replacement. The device still performs well producing ~45 mW for the MOT at the apparatus table, however, the power has declined from original levels of ~65 mW, and all diode lasers eventually fail. Additional BALs sent to be coated at Sacher-Lasertechnik came back with coatings that degraded rapidly over time such that the BALs reverted partially to their lasing state in which they are unusable. An in-house project has been started in conjunction with the Killian lab to produce a coating method of our own to produce replacement BAL units and coat regular diodes to increase their tuning range. Other alternatives to replace the BAL include relatively new tapered amplifier devices available from Toptica which are capable of producing 400 mW of 671 nm light, or replacement with a pair of medium power units such as the HL6555G diodes.

Chapter 3
Field Stabilization and Control

3.1 The Use of Magnetic Fields to Tune Atomic Interaction

Magnetic fields offer the potential to tune the interactions between atoms if they posses a magnetic moment, μ. If a bound state exists between two atoms, then by tuning the atomic energy which varies as $-\mu B$ with the magnetic field (B), it is possible to bring the energy of the colliding atoms into resonance with the bound state energy, giving rise to a scattering resonance called a Feshbach resonance [21–23]. Such resonances exist between different states of lithium, of particular use are those that occur between two atoms in the F = 1, m_F = 1 state of ^{7}Li and the F = 1/2, m_F = +1/2 and m_F = -1/2 states of ^{6}Li.

Fig. 3.1 shows the scattering length vs field for ^{7}Li, as calculated using the coupled channels code of Ian McAlexander [16], updated by post-doc Michael Jack using new data [24] to more closely agree with experimental data. Of particular interest is the zero crossing near 530 G and the Feshbach resonance at 730 G. The zero crossing is useful for experiments involving the production of solitons [25, 26] where small attractive interactions are needed, and disorder-induced localization experiments where the scattering length simply needs to be very small. Feshbach resonances are useful for the production of large stable BECs [2] which are the starting point of many experiments with ^{7}Li, studies on the effect of density on photo-association rate in ^{7}Li [27], and the BEC-BCS crossover in ^{6}Li [28].

For these experiments it is necessary to change the field to values near the zero crossing and Feshbach resonance quickly and accurately, motivating fine control and stability of the magnetic field, and thus the current which produces it.

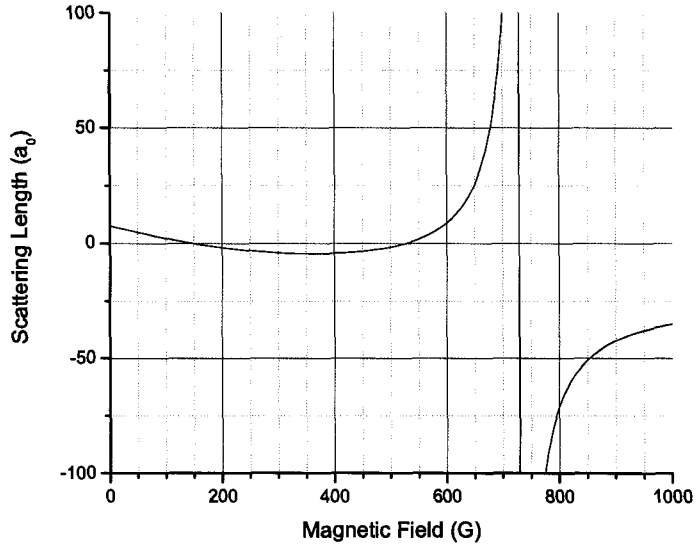

Figure 3.1 Scattering length vs field for two atoms in the F = 1, $m_F = 1$ state of ^{7}Li. Zero crossing are visible at 150 G and 530 G, with a Feshbach resonance at 730 G.

3.2 The Old Scheme

Model 80-185-11-D Lamda-EMI ESS power supplies are used to provide the current for the magnetic trap (50A) and bias coils in the high-field. High field values can be in excess of 920 G requiring currents $\geq$150 A. The supplies can be controlled by means of an external voltage applied to the supply which sets the voltage and current limits. Up until now, the limits of the supply have been relied upon for stability, and the supply either switched on and off rapidly using MOSFETs (referred to simply as FETs throughout this thesis - a description of MOSFET operation can be found in Appendix A) controlled via TTL lines with a rise time of 300 ns, or ramped slowly up by changing the external voltage hooked to J1 connectors on the rear of the supply (with the supplies wired in "external voltage control" mode [8]).

The magnetic trap used is an Ioffe-Pritchard magnetic trap which consists of (anti-) bias coils (referred from here on simply as the bias coils) in Helmholtz configuration with a set of smaller coils inside each of the bias coils called the curvature

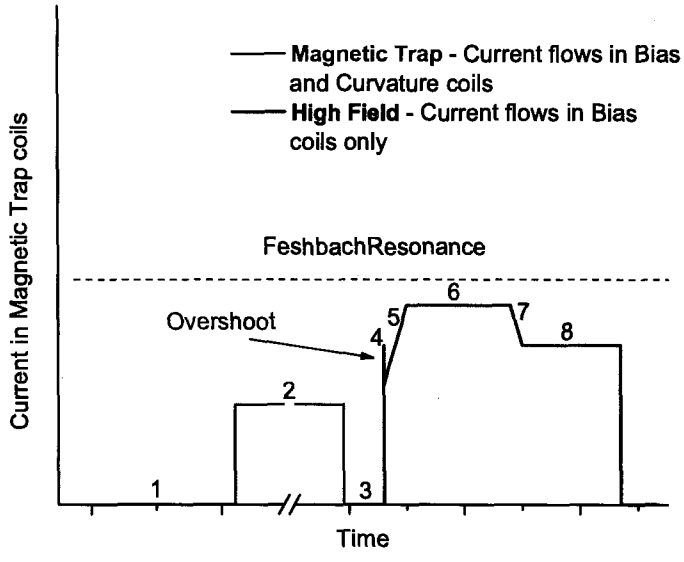

Figure 3.2 Timing of the old sequence. A schematic showing the variation in current in the bias-curvature coils during a typical experimental run: 1. The MOT is loaded and cooling and compression/M_F pumping performed. No current flows in magnetic trap coils. 2. The magnetic trap is turned on in current limit mode by applying 15 V to the gate of FETs in series with the coils. The bias-curv coils which are in series turn on in 2.5 μs. The quad coils are slower but still turn on in under 100 μs. Evaporative cooling is performed in the magnetic trap followed by ramping on an optical-dipole trap produced by focusing $\sim$3 W of 1030 nm light down to a beamwaist of $\sim$30 μm. The magnetic trap is turned off taking 250 μs to settle. 3. Supply settings changed to high-field settings. 4. The bias coils are energized alone with the supply in voltage limit mode by switching a FET. The current overshoots and comes back down to the voltage limit. 5. An arbitary wave form generator is summed into the pin on the J1 connector of the supply which controls the voltage limit, ramping the supply up until it reaches the current limit. 6. Details vary but generally include evaporation in optical trap. 7. Depending on experiment field may be ramped down (using the arbitrary waveform generator) to zero-crossing or another field to image. 8. Field is held at lower field value before switching the gate voltage of the FETs in series with the coils to switch off the current. Turn off takes approximately 250 μs as with the magnetic trap.

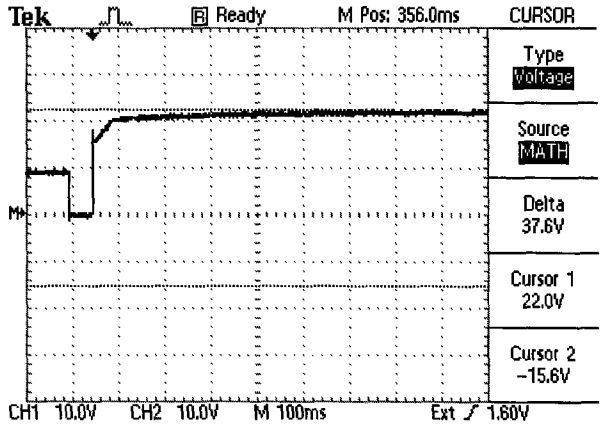

Figure 3.3 An oscilloscope trace showing the voltage across the bias coils for for a typical sequence. The first part of the trace shows the turn off of the magnetic trap followed by the delay labelled as (3) in Fig. 3.2. This is followed by the ramp to high-field (~700 G), during which the overshoot of the field can be seen.

(curv) coils. The axial field from the bias coils nearly cancels the axial field from the curvature coils at the trap center. The curv coils produce substantial axial curvature, however, which provides axial confinement for atoms which are chosen to be low field seekers (in our case the F = 2, $m_F = 2$ state of ^{7}Li). Radial confinement is provided by the quadrupole (quad) coils which consist of a set of 4 D-shaped anti-Helmholtz coils on both sides of the chamber. (A detailed description of the coils with construction instructions can be found in Ref. [8].) A nominal timing sequence for the control of the supplies is show in Fig. 3.2.

Fig. 3.3 shows a zoom in of the high-field ramp of a typical sequence. The overshoot for this ramp is approximately 10% of the total ramp corresponding to 70 G. Attempts to ramp directly to high field values near the Feshbach resonance at 730 G without use of the two stage ramp resulted in heavy losses due to overshoot through the Feshbach resonance where the atom-atom interactions (and thus loss rates) become very large. The two stage ramp prevented heavy atom losses, but the field still overshot and the current could only be ramped to values between the current and voltage limits. The shortest the linear ramp ((5) in Fig. 3.2) could be made was

≈10 ms giving a slew rate of 15 G/ms. We decided to implement an active feedback system based on a current transducer to streamline control and improve the ramping speed and current stability.

3.3 The Ultrastab 866 Current Sensor (The "Danfysik")

The Ultrastab 866 current sensor, made by Danfysik in Denmark (and sold by GMW in America) is a high precision current sensor (see the "Ultrastab 866 Precision Current Sensor" manual). The sensor is capable of measuring currents up to 600 A with a bandwidth of 100 kHz and <2 ppm short stability and <1 ppm stability long term. The output current noise of the sensor is rated at <1.2 μA over a 10 kHz bandwidth range.

For our uses (where the current never goes higher than 150 A) we wrap the cable twice through the center hole of the sensor to increase signal size and relative sensitivity. The ("primary") current flowing through the center hole produces a flux inside the sensor head, which is detected by a flux sensor. The sensor head produces a current in its internal windings, producing a flux opposing that of the primary current at the sensor. (This necessitates that the primary current flow in only one direction denoted by an arrow on the sensor head, or permanent calibration errors may occur.) The sensor detects and maintains the current in the internal windings such that it reads zero net flux, making the internal, or "secondary current" proportional to the primary current, though in a more manageable 0-400 mA range). The secondary current is available as an output from the sensor head and can be used as the input to a feedback circuit.

3.4 The Feedback Circuit

Fig. 3.4 shows the feedback circuit, which takes the input from sensor head. The sensor is connected to the circuit by a shielded cable, grounded at one end to prevent ground loops. The current output from the sensor drops across a 10 Ω (5

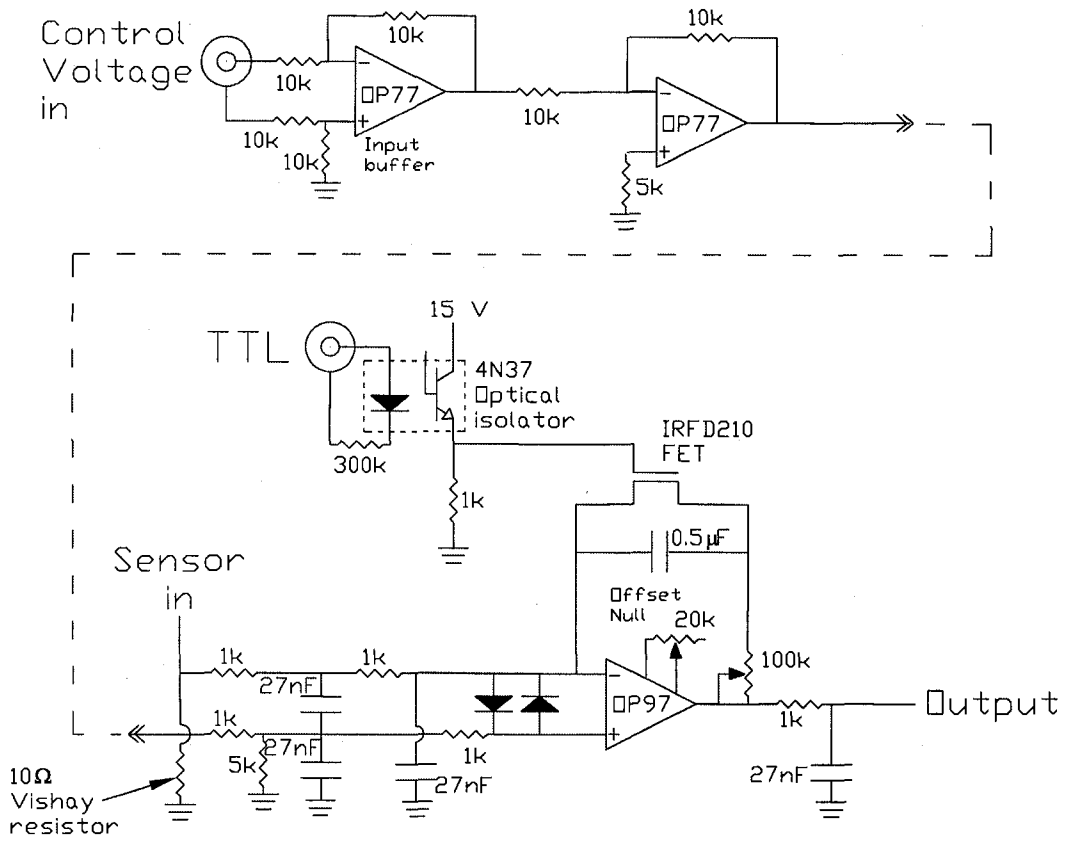

Figure 3.4 The Feedback circuit. Connections from the ±15 V to the OP97 op-amps are biased with 1 μF tantalum capacitors located at the leads of the op-amp to reduce noise.

ppm/ °C) Vishay resistor producing a voltage proportional to the primary current at the inverting (-) input of an OP97 op-amp. Values other than 10 Ω can be chosen, however, 10 Ω provides the largest voltage drop within the range of primary current we operate at, such that the sensor can drive the needed secondary current through the load resistor.

The control voltage is buffered to protect the source and isolate it from the control circuit by a pair of inverting amplifiers with unity gain, the later of which is connected to the non-inverting (+) input of the OP97 op-amp in the feedback loop. When a control voltage is applied, the OP97 will output a voltage in an attempt to equalize the voltage at its two inputs. There are two potential feedback loops - a local loop

that provides integral gain, and an external loop that must be connected to a control element capable of changing the primary current the sensor reads.

If at any time the feedback is not working correctly such that the inputs of the feedback op-amp cannot be balanced, the output will rail. This occurs anytime the feedback is not able to control the primary current, even if no control voltage is applied. This can cause problems if control of the primary current is passed to the circuit and the output is railed as the output cannot instantaneously switch to zero - the output will rapidly decrease to zero (and may ring) but a momentary surge in primary current will occur. Simply putting a reasonable resistor in parallel with the capacitor to provide feedback at DC caused significant drift in the primary current ($\sim$50 mG/s) which was unacceptable for stability.

The problem was fixed by the addition of a IRFD210 FET in parallel with the feedback capacitor. When the FET is conducting the intergrating capacitor is zeroed and control of the primary current can be transferred to the circuit without undesired behavior such as ringing. When switched to non-conducting ($\sim 10^{12}\Omega$) the feedback circuit can control the primary current as needed.

Control of this FET is done by a TTL line buffered with an optical isolator to prevent offsets due to subthreshold leakage through the FET. Without optical isolation significant (and variable) voltages could be observed between the inputs of the feedback op-amp resulting in irreproducibility of primary current for a given control voltage.

3.5 The Control Scheme

Fig. 3.5 shows the overall layout and connection of the system. The cases of the circuits involved in the feedback system are each grounded by a grounding strap connected to the case of the ESS power supply in a star arrangement (necessary to minimize noise in the system). Circuit boxes are isolated from the cases/racks that

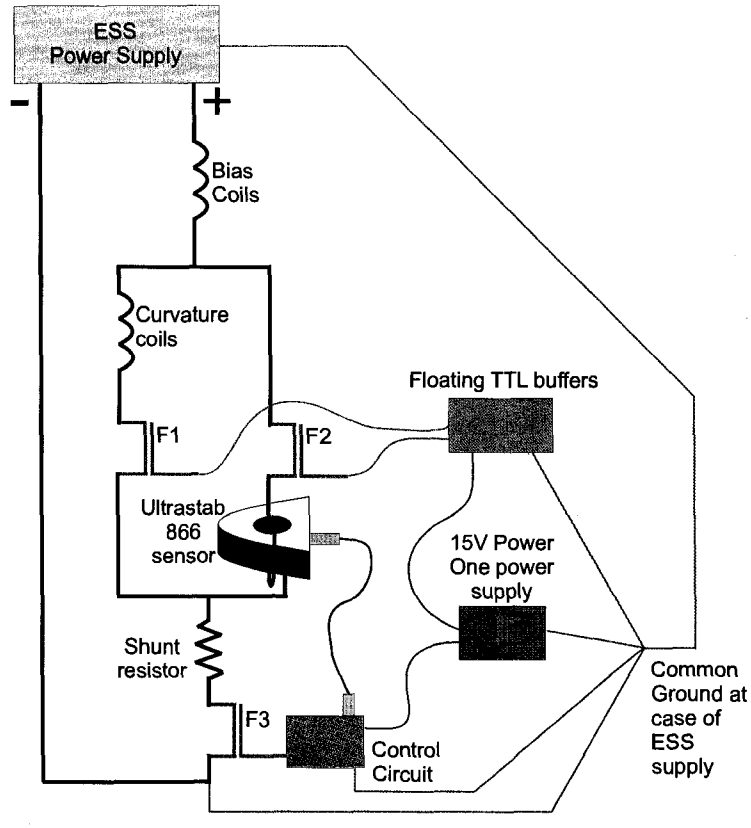

Figure 3.5 The system layout. FETs 1-3 are IXFN180N20 MOSFETs.

support them so that the only connection to ground is the ground strap. Where connections between circuits are made, shielded cables are used with the sheath connected at one end only to prevent ground loops. In the case of our system incorrect grounding can result in noise at the level of several parts in 10^3 corresponding to $\sim$1 G in the high field which is totally unacceptable.

The element controlled by the feedback for the system is a pair of IXFN180N20 FETs. Insulated gate bipolar transistors (IGBTs) are another option (and would most likely work) but are more suited to higher voltage applications (>500 V) [29]. Additionally we had IXFN180N20 FETs available as they were used in the past to switch the quad coil current but have since been replaced by IXFN230N10 FETs,

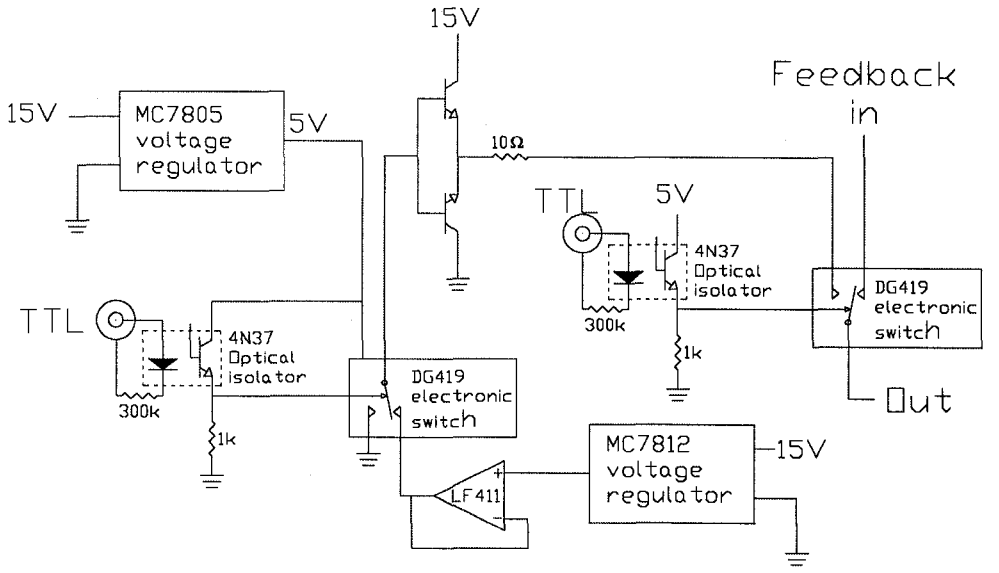

Figure 3.6 This circuit provides a means to switch between control of F3 by a TTL line and control via the feedback circuit. It also buffers the control lines for protection and rapid turn on of the magnetic trap.

making them a natural choice.

The FETs shown in Fig. 3.5 are drawn as single devices but are actually pairs in parallel with a common control voltage. The FET (pair) controlled by the feedback is labelled F3 and is operated both in "digital mode" (magnetic trap configuration - the gate-source voltage, $V_{gs} = 0$ or +15 V) and "analog mode" (high-field) using the feedback circuit. In "analog mode" the voltage applied to the gate of F3 is varied continuously to vary the resistance of the FET which in turn changes the current in accordance with Ohm's law (with the supply is in constant voltage mode).

The circuit which controls whether F3 is operated in digital mode or by the feedback circuit is shown in Fig. 3.6. A TTL line controls a DG419 electronic switch which selects digital and analog control modes. Another DG419 controls the state of F3 when operated in digital mode. A push-pull pair buffers the output to allow rapid switching of the IXFN180N20 FETs which have an input capacitance of around 22 nF each (44 nf for two in parallel).

FET (pair) F1 and F2 are used to select whether current flows through both the bias and curvature coils (magnetic trap configuration), or the bias coils alone (high-field). The magnetic trap is turned on/off in the experimental sequence by togging the state of F1 open/closed with F3 in digital mode and set to open (with F2 closed).

To enable high-field configuration, F1 is closed and F2 opened (to bypass the curvature coils) with the state of F3 set closed so no current flows. Control of F3 is set to analog, and some time later a TTL triggers a 33220A arbitrary function generator (arb) which provides the control voltage for the feedback circuit, which supplies the needed gate voltage to F3.

The turn on and off of F1 and F2 are not entirely straightforward due to the fact the sources of these FETs are not at a fixed voltage. Depending on the state of F3 the source of F1/F2 can be either at ground or the supply limit (80 V), with a voltage equal or below that of the source turning off the FETs and a voltage somewhat higher than 6 V turning the FETs on. Moreover, the IXFN180N20 FETs can only handle a V_gs as high as 30 V transiently, and 20 V steady state, preventing the use of large static voltages for the turn on/turn off. The solution to this problem was to build floating buffers based around WPC10R24S12 chips which take 24 V and output +12 V with respect to a center pin which can be tied to some floating voltage. The buffers are simplified versions of the CMOS buffers shown in [5, 8] and take in a signal from a TTL line which is decoupled from the floating section of the board using 4N37 optical isolators. The 4N37s are buffered by TIP120/125 push-pull pairs which provide the current for fast switching of F1/F2 ($\approx$200 ns). The layout of the buffers is shown in Fig. 3.7.

Some care must be taken in setting the supply limits correctly to their magnetic trap and high-field settings. The circuit used to do this is shown in Fig. 3.8. Independent control voltages for both the current and voltage limits in magnetic trap and high-field configurations are derived from 10 turn Clarostat potentiometers connected

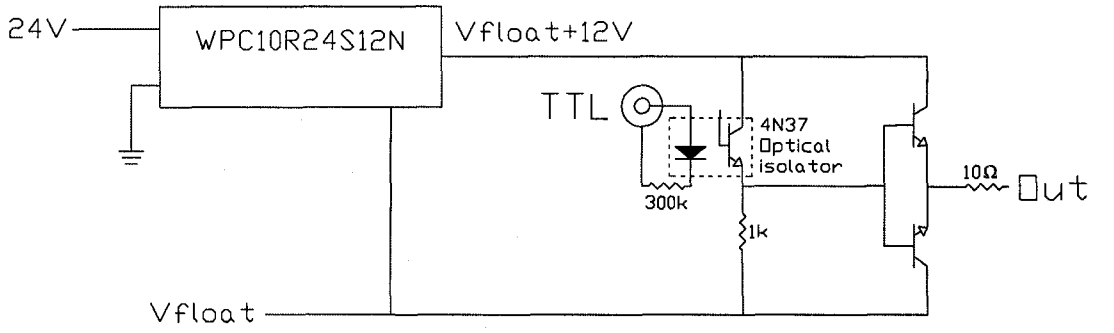

Figure 3.7 The circuit layout of the floating buffers. These buffers provide turn on voltages for F1 and F2 with respect to the voltage at their common source. Both F1 and F2 have separate buffers, each with their own WPC10R24S12 chip for fast switching of the FETs.

to temperature stabilized LM399 precision voltage sources. A TTL line switches two DG419 electronic switches between different supply settings, with the TTL lines optically isolated to protect control electronics from the supply. The rails of the circuit are supplied by WPC10R24D12N chips which are dual output versions of those used in the Fig. 3.7, used here to isolate the ground of the control circuitry of the supply from the negative power terminal.

To set the limits for the magnetic trap configuration the FETs must be set for magnetic trap operation with the TTL line that controls the supply limit control circuit (Fig. 3.8) low and the set point pots for both current and voltage at minimum. The voltage limit and current limit are then simply increased by adjusting the pots until the current limit is ~50 A with the voltage limit just above it so as to be in current limit mode.

Setting the limits for high-field is more complex, however, as sufficient voltage is needed to drive the current to produce a desired field, but the higher the voltage limit is set, the more power will be dissipated by F3. The IXFN180N20 FETs are rated to handle 700 W, but to be safe we operate below this due to limitations in the conductivity of the cooling plates and to be sure no FETs are destroyed. The TTL

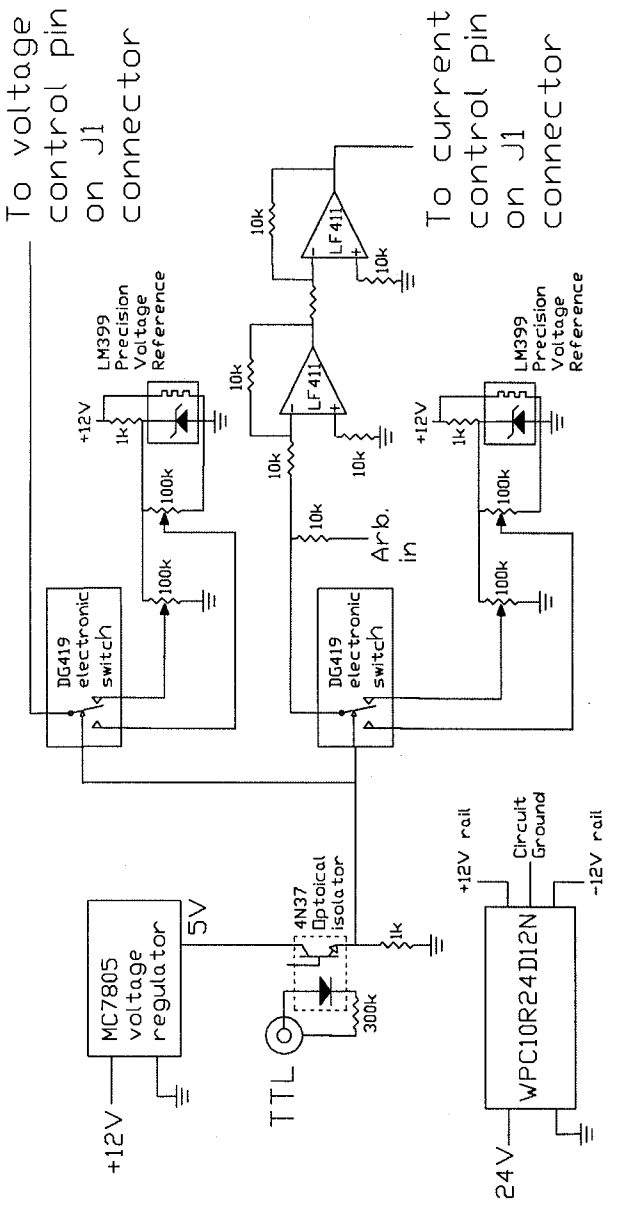

Figure 3.8 The supply limit control circuit - the output of this circuit connect to the J1 connector on the back of the supply and set the voltage and current limits. The current limit set point has an input allowing an arb to be summed in in order to control the current as described in 3.2. The 24 V connection to the WPC10R24D12N chip is biased with a 1 μF tantalum capacitors to reduce noise.

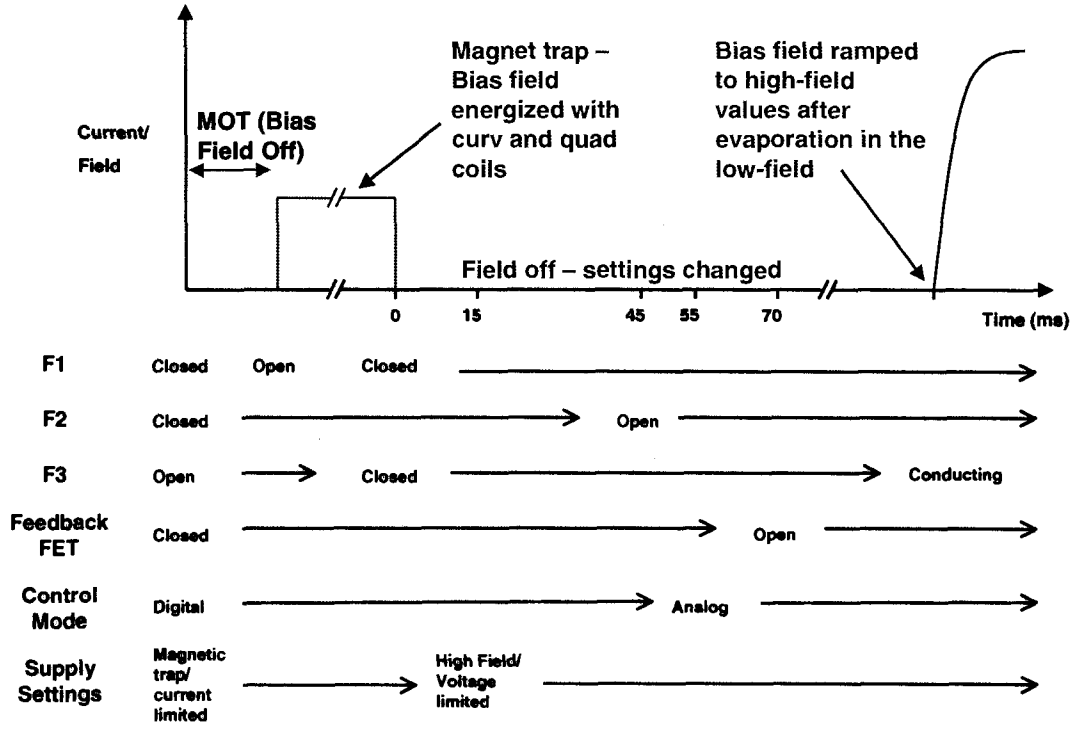

Figure 3.9 The timing sequence for switching the supply settings, FETs, and triggering the ramp to the high-field with the Agilent 33220A Arb.

line to the supply limit control circuit is set high with the current limit and voltage limit set low. The voltage limit is turned up from zero with control of F3 in digital mode and current flowing through F2 as in the high-field configuration. The voltage is turned up until the desired current flows then set $\sim$1 V higher so the resistance of the FET can be made non-zero as in analog-control mode. The current limit which is necessarily set higher so the supply is in voltage limit mode, is set $\sim$5 A above the voltage limit so that in the event of a short or catastrophic failure the coils are not damaged.

3.6 The New Sequence

Timing for the new sequence is shown in Fig. 3.9 and described below.

The cabling for the MOT is essentially unchanged and it is turned on and off as

in the timing diagram of section 3.2 above, with CMOS buffers as shown in Ref. [8]. The buffers can supply more current and higher voltage than the TTL lines which control them, and allow fast switching of the IXFN340N07 FETs which control the MOT current.

The quadrupole (quad) coils are also independent from the feedback system and as such can be controlled in the same way as the MOT coils, with IXFN230N10 FETs used due to the lower current requirements. The wiring and switching schematic for the quads can be found in Ref. [5].

The sequence differs where control of the bias and curv coils are concerned. At the very beginning of an experimental run both F1 and F2 are closed, and F3 set fully open in digital mode until after the magnetic trap. The FET in the feedback circuit is conducting with the control voltage for the feedback at 0 V locking the output of the feedback circuit to 0 V. The supply is set to the magnetic trap settings in current limited mode at 50 A using the circuit of Fig. 3.8.

The magnetic trap is turned on by simultaneously energizing the quad coils, and making F1 conducting to pass current through both curv and bias coils. An optical-dipole trap is ramped on a few hundred milliseconds before the magnetic trap is turned off to prevent the atoms being lost. F1 is closed to turn off the magnetic trap, followed by F3, which is still in digital mode. 15 ms later the settings on the ESS supply are changed from their magnetic trap settings to the high field settings in voltage limited mode. 30 ms after switching the supply settings F2 is opened, and a further 10 ms later control of F3 switched over to the feedback circuit. With F2 open the feedback circuit is in control of the primary current, and the FET in the local feedback loop can be closed without any surges in the current. We do this 15 ms after switching to analog mode, and trigger the Agilent 33220A arb which controls the the feedback circuit a few milliseconds later.

The Agilent 33220A arb can be programmed be either the front panel or by using

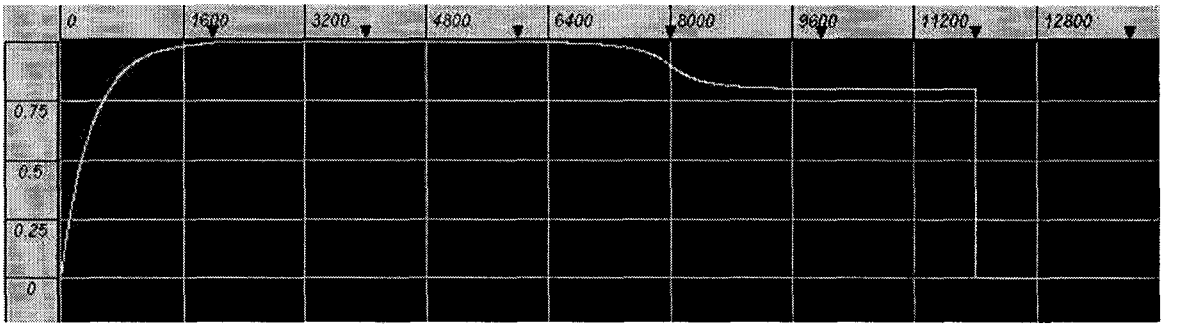

Figure 3.10 The IntuiLink software interface. The waveform shown is typical of that used in our experimental sequences.

the IntuiLink software that comes with the device. An example waveform is shown in Fig. 3.10. The current is ramped up using an exponential rise, generally to somewhere near the Feshbach resonance. The use of exponential waveforms eliminates the sharp points associated with changing slopes rapidly which can cause ringing. The field may then be ramped further up or down, or simply turned off, depending on the experiment.

After imaging the atoms the sequence is at an end. Typically we write waveforms longer than needed, and switch off the high-field by switching F2, though in principle the field could be ramped down using the feedback. Since, however, the arb and *Control* (our computer control software) are independent, it is more convenient to simply change the timing in *Control* and use the former method to switch off the field.

3.7 Ramping Performance

The Danfysik feedback system can be used to execute arbitrary waveforms as shown in Fig. 3.11.

Fig. 3.12 (a) shows the first part of a waveform as shown in Fig. 3.10, by measuring the voltage across the bias coils. It shows a 15 ms ramp from 0 G to 710 G over 15 ms. The average slew rate is 47 G/ms, with the peak slew rate closer to 70 G/ms. Fig.

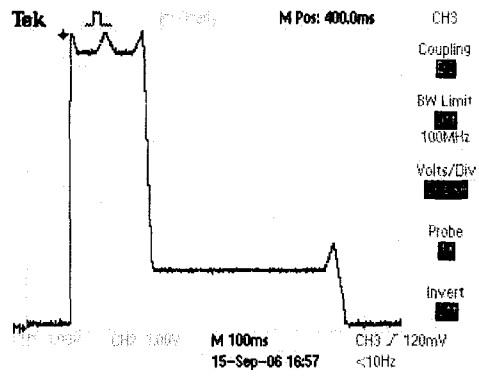

Figure 3.11 An example of a more complex waveform the feedback system can be used to execute. Such waveforms are easy to create by programming an arb.

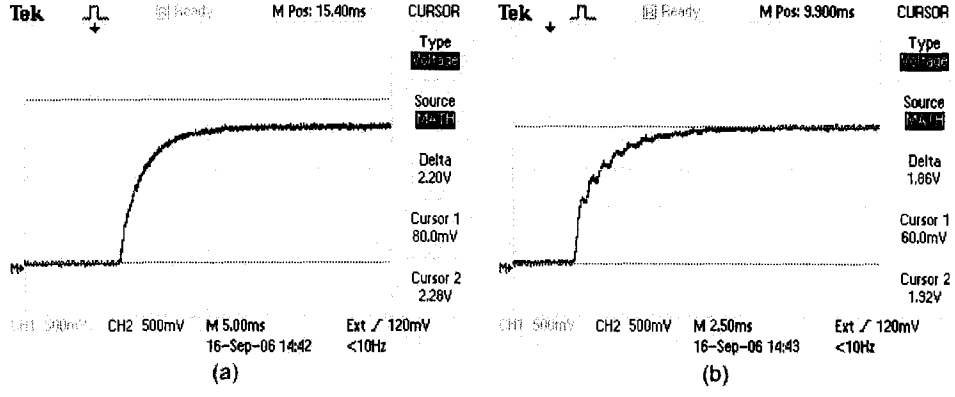

Figure 3.12 Three field ramps to 710 G showing: (a)A 15ms exponential rise with the current following the waveform well, (b) A 10ms exponential rise with ringing

3.12 (b) shows what happens when the waveform used is compressed to be shorter than 15ms - the feedback circuit cannot change the field rapidly enough to keep up with the control voltage and ringing occurs.

3.8 Stabilization

A good way to measure the stability of the field is to use the linewidth of RF transitions between the F = 1, $m_F = 1$ and F = 2, $m_F = 2$ Zeeman sub-levels of the hyperfine structure of ^{7}Li. These states are very long lived with sub-Hertz linewidths, well below the resolution of the measurement. Other broadening mechanisms include

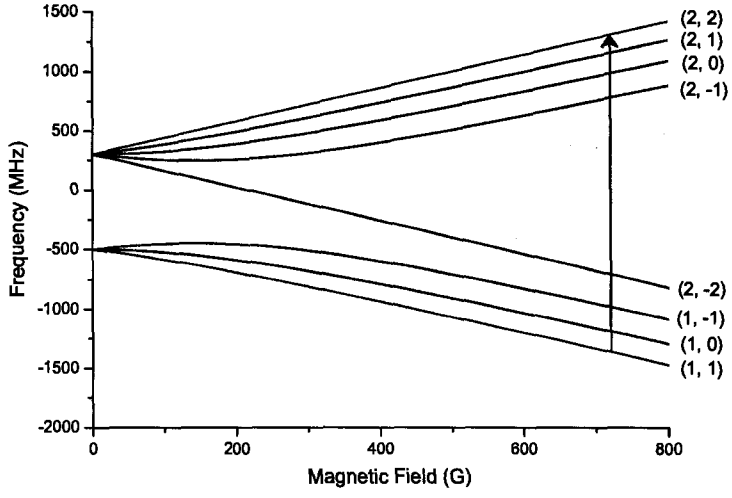

Figure 3.13 The Zeeman sublevels of the $2\,^2S_{\frac{1}{2}}$ level of ^{7}Li as a function of field. Energy levels are labelled as (F, M_f). The F = 1, M_F = 1 to F = 2, M_F = 2 transition is shown by the red arrow.

noise on the field, thermal broadening, and finite linewidth of the HP8648C RF synthesizer used to perform the state transfers. The linewidth of the synthesizer is not given but is assumed to be of order of the accuracy of the device which corresponds to 1.5×10^{-6} of the output frequency, or approximately 4 kHz.

Each point of the resonance requires the sequence to be repeated over as absorption imaging is destructive. This is an advantage over a purely electronic measurement as it samples both the stability and the repeatability of the final field which both contribute to uncertainty as far as real experiments are concerned.

Fig. 3.13 shows the variation of the F = 1, $m_F = 1$ to F = 2, $m_F = 2$ transition with field. At low fields where the Zeeman effect is smaller than the hyperfine splitting, the states are well described by the quantum numbers F and M_F and vary with field according to

$$E = g_F \mu_B B M_F \tag{3.1}$$

(where g_F is the Landé g factor for the hyperfine structure, μ_B is the Bohr magneton), such that the transition frequency between these two states varies at a rate of

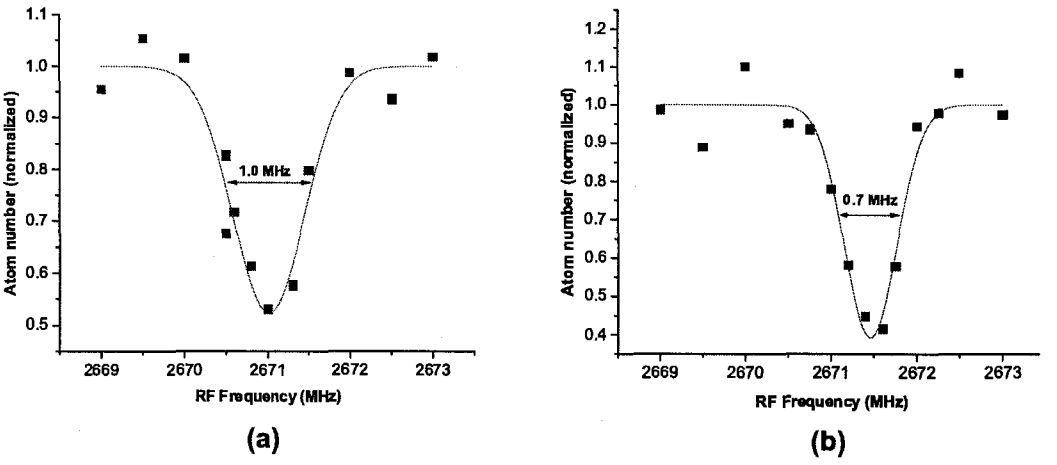

Figure 3.14 RF resonances for the F = 1, $m_F = 1$ to F = 2, $m_F = 2$ transition of ^{7}Li at 721 G with (a) the current limit of the supply controlling the field, and (b) active stabilization using feedback from the Ultrastab 866 current sensor. The small difference in the position of the resonance is due to limitations in how accurately the field can be reproduced in switching between the two modes.

2.8 MHz/G. At higher fields where the Zeeman effect is larger than the hyperfine interaction, the nuclear and electron spins precess individually around the field, and F ceases to be a good quantum number. In this regime the good quantum numbers become M_I and M_J, and the energy is given by

$$E = g_J \mu_B B M_J + A M_I M_J \tag{3.2}$$

(where g_J is the Landé g factor for the fine structure). Since the F = 1, $m_F = 1$ and F = 2, $m_F = 2$ states are pure states the slope is expected to be the same in both the low and high field, and inputting the relevant quantum numbers into Eqn. 3.2 yields 2.8 MHz/G as expected.

Fig. 3.14 shows two RF resonances taken for transfers from the F = 1, $m_F = 1$ state to F = 2, $m_F = 2$ state. The atoms were transferred from the magnetic trap to the optical trap after RF evaporation which cools the cloud to $\approx 4\ \mu K$. The atoms were transferred from the F = 2, $m_F = 2$ state (the state used for the magnetic trap) to the F = 1, $m_F = 1$ state by a broad RF sweep in the low field. The field was

ramped up to 721 G by a simple exponential rise where it was held until the atoms were imaged. The power in the optical trap was lowered inducing forced evaporation, shrinking the cloud and reducing it's temperature below T_c, the critical temperature for a BEC to form. 500 mW of RF power was applied by switching on the HP8648C synthesizer remotely using GPIB and amplifying the output using a Minicircuits amplifier. An RF switch was used to ensure the duration of the RF pulse was not affected by the timing jitter inherent to GPIB. A linear voltage ramp was applied to the frequency modulation port of the synthesizer so that the output frequency of the synthesizer would sweep over a range of 200 kHz. The initial frequency of the sweep was varied around the expected location of the RF resonance to map the width.

Fig. 3.14 (a) is a resonance taken without stabilization. The resonance has a full width half maximum (FWHM) of $\sim$1.0 MHz corresponding to a stability of 0.36 G, or $\sim$50 parts in 10^5. Fig. 3.14 (b) shows a resonance with active stabilization which fits to $\sim$0.7 MHz, or 0.25 G corresponding to 35 parts in 10^5. Resonances were roughly located using 400 kHz sweeps before switching to 200 kHz sweeps to take more accurate resonances. No significant decrease in width was observed changing from 400 kHz to 200 kHz.

The measured stability for the supply/unstabilized case is consistent (slightly better) than it's rated stability of 75 mV_{p-p} on 80 V corresponding to $\approx$66 parts in 10^5. Unfortunately the stability of the field in the stabilized configuration (while better than the supply limit) was significantly worse than $\leq$1 part in 10^5 implied by the RMS current noise specification of the sensor (given a 10 Ω resistor).

Intrinsically, the stability of the field is ultimately limited by the repeatability and stability of the Agilent 33220A Arb and the noise on the Ultrastab 866 sensor which provide the inputs to the circuit. The sensor is specified to an accuracy of $\approx$2 ppm, with an RMS output noise of $<$1.2 μA over a range of 10 kHz. The arb is specified to 1 mV_{p-p} accuracy, or 3 parts in 10^4 on a 2.8 V signal (which produces a field of

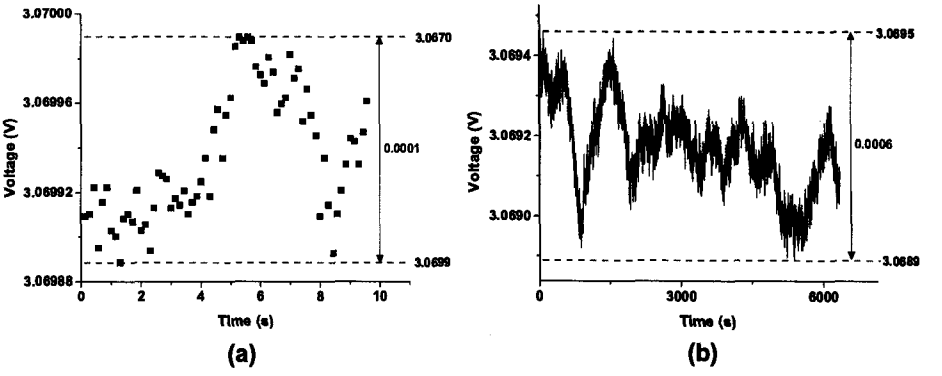

Figure 3.15 Data taken with an Agilent 34401A precision DMM showing the variation in the voltage produced by the Agilent 33220A arbitrary waveform generator used to control the feedback circuit. (a) The voltage is ramped to 3.07 V and held there for 10s. The noise on the level is 0.0001 V. (b) The voltage is again ramped to 3.07 V, but repeatedly over an extended period. In addition to the noise associated with a single ramp, the variation in the high voltage over an extended period can be seen and is observed to be 0.0006 V.

691 G). The arb then sets the practical limit for the width of the resonances, and is very close to the value observed.

Very often, however, equipment exceeds it's specification. Fig. 3.15 (a) shows the voltage as measured with an Agilent 34401A precision DMM, after ramping the arb from 0 to 3.7 V and holding the high level for 10 s. The data was dumped to a file using the GPIB interface on the DMM. The high level is seen to vary by 0.0001 V, corresponding to 3 parts in 10^5 on a 3.07 V signal. This was repeated several times and is consistent with the other runs, and is representative of the noise for a single ramp on the timescales used in the experimental sequence. Fig. 3.15 (b) shows the results of ramping the voltage on the arb to 3.07 V repeatedly over an extended period. The period of the waveform was 1 s, similar to that used in an experimental run. Fig. 3.15 contains many ramps to the high level and shows the variation in the maximum level over an extended period on timescales consistent with making a resonance (consisting of many shots each of which takes 1-2 minutes each). The level is seen to vary by 0.0006 V, or 2 parts in 10^4.

Instability/drifting of the output voltage from the arb is thus sufficient to explain a

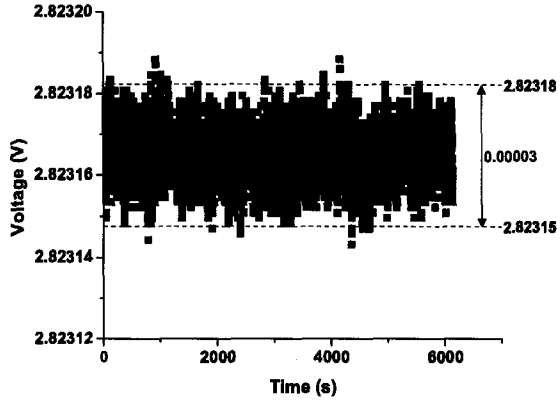

Figure 3.16 The output of the capacitor-charge based ramp circuit over an extended period. The 3×10^{-5} V variation in final voltage level over this period corresponds to 1 part in 10^5.

significant portion of the observed width of the resonance, and improving the stability of the control voltage is clearly the first issue to address to get a truer measure of the performance of the circuit. A simple ramp circuit was constructed utilizing the charging of a capacitor to ramp the current to the high-field over 50 ms. The circuit used the output from an LM399 as a reference, reduced from 7 V to 2.8 V by a voltage divider formed by a pair of 5ppm/ °C resistors. The resulting output voltage ramped the field to 691 G when used as the control voltage for the feedback circuit. The long term noise/drift of the circuit was measured using the Agilent 34401A DMM and is shown in Fig. 3.16.

Evaporation in the optical trap was performed to produce a bimodal cloud with a condensate fraction of ≈70% containing ≈200,000 atoms. An RF sweep of 150 kHz was applied to transfer atoms from the F = 1, $m_F = 1$ state to the F = 2, $m_F = 2$ state where upon the cloud was released from the trap for a time of flight of 0.7 ms and imaged by absorption. The resonance (shown in Fig. 3.17) fits to a FWHM of 222 kHz or 82 mG corresponding to 12 parts in 10^5 - a 300% improvement over using the arb and over 400% compared to the old control scheme.

The noise spectrum of the stabilized supply was analyzed with a SRS 780 network

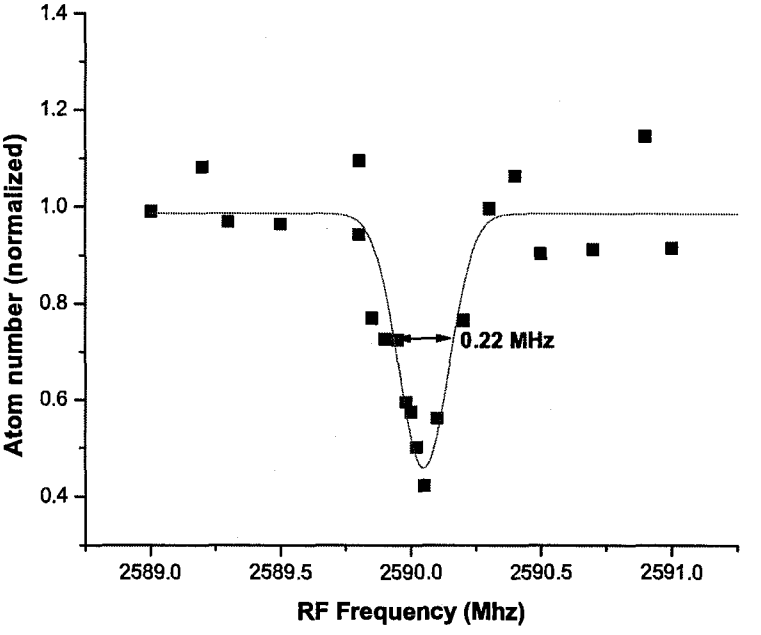

Figure 3.17 An RF resonances for the transfer of atoms from the F = 1, $m_F = 1$ state to the F = 2, $m_F = 2$ state of ^{7}Li at 691 G using feedback from the Ultrastab 866 sensor and a home made ramp circuit.

spectrum analyzer, measuring the voltage drop across the the 10 Ω Vishay resistor which drops the output of the Ultrastab 866 current sensor. The spectrum for frequencies below 1.6 kHz is shown (beyond which the spectrum is essentially flat) for the cases the control voltage is provided by the Agilent 33220A arb and the home made control circuit (see Fig. 3.18). At low frequencies additional noise can be observed for the case the Agilent 33220A arb is used.

Summing the power over the spectrum (for the case of the home-made ramp circuit) and converting to an RMS voltage gives ≈7 parts in 10^5, which accounts for most of the instability in the field as measured using the RF resonance method. Clearly the RF sweep used will contribute significant broadening to the resonances and is sufficient to account for most of the difference between the two methods. Other sources of broadening include thermal broadening, broadening due to curvature of the magnetic field (which I estimate to be ≈5 kHz for each source) and broadening due

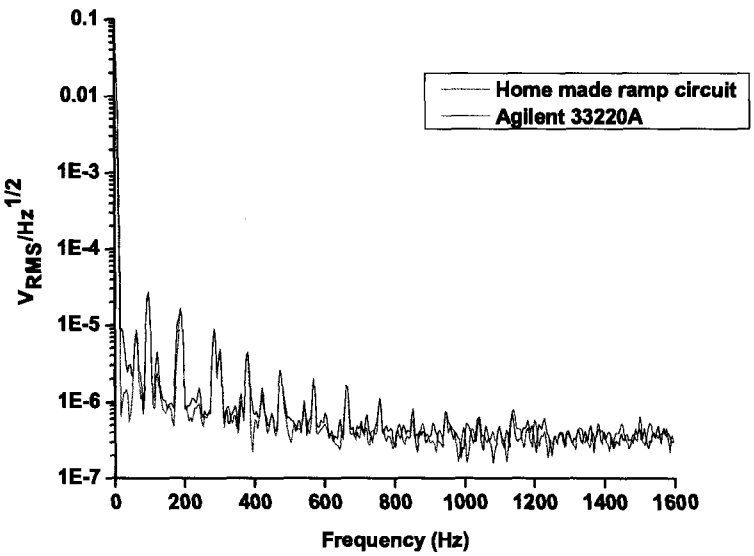

Figure 3.18 Noise spectrum of the high-field current as measured by the Ultrastab 866 sensor on a 1.6 kHz scale with a 4 Hz bin size. The green trace shows the noise in the case of the home made ramp circuit is used. Red shows the noise when the Agilent 33220A arb is used.

to the linewidth of the synthesizer.

The spectrum is dominated by peaks at 60 Hz and 96 Hz (and their harmonics). The former can be observed if the SRS780 is used simply to measure the noise on a 8 Ω 1 W resistor and seem to be either on the instrument itself, or pickup (either way a measurement artifact). It is likely there is some 60 Hz noise on the current since both the feedback circuit and the Lamda-EMI supplies ultimately draw their power from the mains, however, quantifying it with with precision with the SRS780 is not possible. The 96 Hz on the other hand is less common, and is intrinsic to the supply.

A potential source of field instability in the feedback circuit is drift due to current leakage through the IRFD210 FET used to short the feedback when the feedback circuit is not being used to control the current. The current flowing through the bias coils can be measured to 4 parts in 10^5 by measuring the voltage drop across the precision shunt resistor in series with the bias coils and F3. Observing this voltage over the period of a sequence shows no change in the last digit over timescales in

excess of 10 s. As such any such drifts must be in the region of 4 ppm/s or below. Drift of the integrator is therefore small compared to the width of the RF resonances, but is relatively easy to reduce. There exist FETs such as the SST4391 from Vishay which have leakage currents 1000 times lower than the 100 nA of the IRFD210. Alternatively page 224 of Horowitz and Hill (Ref. [30]) suggests an improved method of zeroing the integrator using a pair of FETs with higher leakage currents such that the effect on the intergrator is minimized.

In addition to drift, the IRFD210 represents a potential source for introducing noise into the system. The noise figure for the FET is not specified, but is presumably at a similar levels to that of the leakage current. Reducing leakage by either of the above means should therefore also reduce any noise introduced by the FET as well as reducing drift.

3.9 Summary and Future Work

An improvement in the stability of the magnetic field of approximately a factor of four is observed from $\approx$ 50 parts in 10^5 to 12 part in 10^5 moving from relying on the supply limit for stability to the feedback system, so long as the more stable home made ramp circuit is used. Where the Agilent 33220A arb is used improvements of around 30% are observed with a stability 36 parts in 10^5.

In order to take full advantage of the field stability a more stable arb will be needed than the Agilent 33220A. The ramps used in our experiments are often changed in magnitude, but not nearly so often in functional form. As such there are several different options available for providing a stable control voltage for the field. Agilent manufactures a higher resolution arb (N8241A) with 15 bit resolution (in contrast to the 14 bit of the 33220A). The noise level of the unit is unfortunately not clearly specified, and with the resolution only being a factor of two better than the 33220A it seems unlikely the noise is significantly improved. Another option is to use a more

complex home made circuit, which could involve a range of set points for different fields with (relatively) small trim resistors (to minimize drift) for fine adjustments of the field. Additional ramps could be summed in to ramp down to lower field values like the zero crossing in ^{7}Li if the experiment required it. A third option is a hybrid system utilizing a home made circuit to provide the body of the control voltage and summing in an arb to make fine tune adjustments of the field such that any fluctuations on the voltage output of the arb represent smaller fractional fluctuations in the field. This would also reduce a small issue we have currently where the 1 mV size steps of the Agilent 33220A arb limit us to discreet steps of 200 mG. Whichever solution, it will be necessary to make sure the low frequency fluctuations/drift on the voltage are as small as possible (with 1 part in 10^5 providing a reasonable benchmark) and the high frequency noise relatively low.

Using a stable arb to control the field the observed stability corresponds to 80 mG at 691 G. Both this value, and indeed the 220 mG stability achievable using the Agilent 33220A arb are more than adequate for experiments involving broad Feshbach resonances (like that of ^{7}Li which is $\approx$200 G wide). Where such measurements are concerned the improved stability achievable using a more stable voltage source will manifest mostly in improved repeatability and lower uncertainly. The improved stability has more direct consequences for current experiments involving tuning the field to values near the zero-crossing of ^{7}Li near 544 G. Achieving small a values may allow observation of the force between the magnetic dipoles of the atoms in a condensate which is otherwise dominated by the s-wave scattering force. In addition, small a is important for making the healing length of a condensate large, where the healing length, ξ is given by Eqn. 3.3 (where n is the density).

$$\xi = \frac{1}{\sqrt{8\pi n a}} \tag{3.3}$$

Obtaining a large healing length is thought to be significant for disorder related phenomena such as disorder induced (Anderson) localization [31] where the disorder

length scale must be made shorter than the healing length. In the region of the zero-crossing the scattering length varies linearly with field at a rate of 0.07 a_0/G. Consequently improving the field stability by a factor of four relaxes the constraints on the disorder by a factor of two.

If, however, any future experiments involve working with the narrow Feshbach resonance of ^{6}Li at 543 G which has a width of $\sim$ 400 mG [32], or any of the p-wave Feshbach resonances (at 159 G, 185 G, and 215 G with widths varying from 200-400 mG), it is likely better stability will be needed. Further improvements will require eliminating/supressing the noise at 96 Hz which dominate the residual noise on the spectrum, improving filtering of 60 Hz harmonics and making the changes relating to the zeroing of the integrator (see section 3.8).

Where ramping speed is concerned, the feedback system allows the field to be ramped up at an average speed of 47 G/ms with peak speeds of 70 G/ms possible. This is faster than the old scheme, where speeds $\sim$15 G/ms were more typical, but somewhat slower than schemes available on other experiments [33]. Recent work has been done improving the bandwidth of the feedback circuit from 3 kHz in order to improve ramping speed. The 3 kHz limit was originally imposed to counter noise observed during preliminary testing before it was deployed on the apparatus, however, many improvements have been made since that time. As such it has been possible to increase the bandwidth without introducing any significant noise and hence increase the ramping speed to closer to 3 ms from the original 15 ms. At a ramp speed of 3 ms the system is slew rate limited, with the rate constrained by the current output of the circuit used to switch control of F3 between analog and digital modes. The circuit could be modified to include higher current analog switches such as the FSA2257 or even mechanical relays. Another option would be to current buffer the output of the circuit, though this could potentially introduce noise/drift.

The final option is to remove the analog/digital mode switch circuit entirely,

though this would require more extensive modifications to the apparatus. F3 would have to be bypassed and the output of the feedback circuit switched to the gate of F2. The shunt resistor would have to be moved so that the sources of F1 and F2 were at ground, and the timings in *Control* modified to work with the new sequence. These modifications would simplify the system and allow for faster field ramps, but prevent control of the field in the magnetic trap should the field switching become sufficiently fast to permit good MOT-magnetic trap transfers. Conversion back and forth between old and new control schemes would also be more time difficult, but this capability is no longer necessary since remaining problems with the new system were ironed out.

Appendix A
MOSFETs

A.1 A Brief Introduction to MOSFETs

Metal-oxide-semiconductor field-effect transistors or MOSFETs are type of semiconductor device with a variety of uses including switches and variable resistors in which capacity they are used on our experiments. The IXFN series (made by IXYS and purchased from several companies including Future Electronics and CMB Components) and IRFD210 MOSFETs used in this these are specifically N-channel enhancement mode types. N-channel refers to the devices construction which is described below. Enhancement refers to the fact the device is doped such that a positive gate voltage must be applied to enable conduction between drain and source, as opposed to depletion types which will conduct at gate voltages of 0 V and require negative gate voltages to stop conduction. Fig. A.1 (a) shows full terminal diagram of the IXFN180N20 and other IXFN series FETs with built in protection diode, while (b) shows a simplified version used to represent the same MOSFETs throughout this thesis.

Fig. A.2 shows the construction of an N-channel MOSFET. The source and drain terminals are connected to semiconductor regions highly doped (denoted by the "+") with excess electrons (n-type), with the source also connected to the to the body as shown in A.1. The gate terminal is insulated from a p-type region (a region with a deficit of electrons) by an oxide layer. When a positive voltage is applied to the gate (as referenced to the body) negative charge builds up at the oxide layer which forms a channel connecting the drain and source regions as the voltage is increased. Thus applying a positive gate-source voltage allows conduction between drain and source regions (since the body and source are connected).

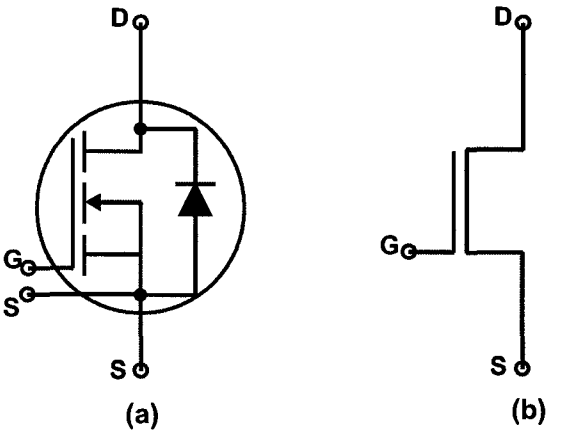

Figure A.1 (a) IXFN series MOSFET connection diagram. G is the gate, D is the drain, and S is the source. (b) The simplified symbol used to represent the more complex MOSFETs used throughout this thesis.

A.2 MOSFETs and the feedback system

While the IXFN180N20 FETs are capable of handling 700 W steady state, the supplies are capable of supplying far more than that and care must be take to program sequences into the arb and in setting the current limits on the supplies as described in 3.5. The problem lies in resistance of the (bias) coils which is sufficiently large (approximately 0.4 Ω) that the supply must be set to 45-50 V (depending on the high-field value) to drive the necessary current. As the field is swept on, the voltage dropped across the FET starts at the supply voltage and sweeps down to some low value necessary to allow the high-field current to flow, somewhere in the region of 1 V. Where the current is very low and the resistance of the FET high, the power dissipated is low. Similarly, where the current is high and the impedance of the FET low, the power dissipated is also sufficiently low for the system to run in steady state for a significant time. In the intermediate regime, however, the power dissipated in the FETs can be very high (for example 50 A $\times$ 25 V = 1250 W) such that if run at these values for a significant time the FETs will be damaged and require replacement.

Using pairs of matched FETs helps protect against damage, but in practice no two

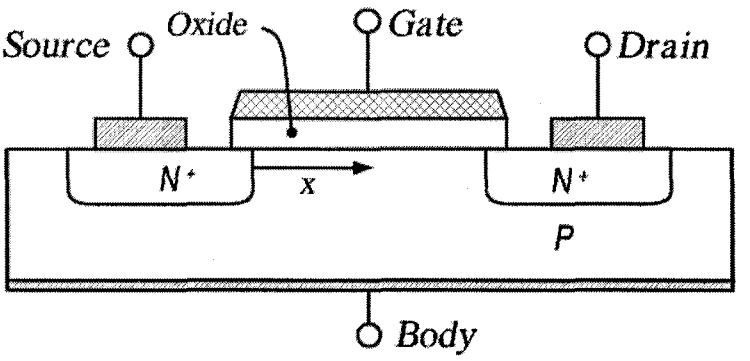

Figure A.2 The construction of an N-channel MOSFET [34]

FETs are identical, and the cost (approximately fifty dollars) of the FETs precludes purchasing large numbers of devices to find the perfect match. Experimentation has shown pairs of reasonably matched FETs to be reliable over many months so long as care is taken to ramp up to final values in no more than a few seconds, though milage will vary depending on how well FETs are matched (so far 5-6 s has not proved a problem the pairs that have been used - producing a more solid figure would both be expensive and time consuming). Similarly, if the field is ramped back down to a lower value before turn off no problems have been seen so long as the field is not held at the lower value for too long. Since typical high-field sequences are $\sim$ 4s, heating thus far has not proved a problem.

Fig. A.3 shows the variation in drain current with gate voltage. Conduction in this case start at 3.75 V, but can vary by up to a volt [30] which covers much of the range over which conduction occurs. Picking two random FETs to pair can result in one servoing almost all the current (and hence power) and the other almost non at all.

In order to keep power dissipation to acceptable levels, the voltage on the supply is set such that the FETs operate in a regime where the resistance is fairly low, which would be around 5 V for the FET shown in Fig. A.3. If the supply voltage is not set correctly, it is possible for the feedback circuit to forced to be operate the FET in

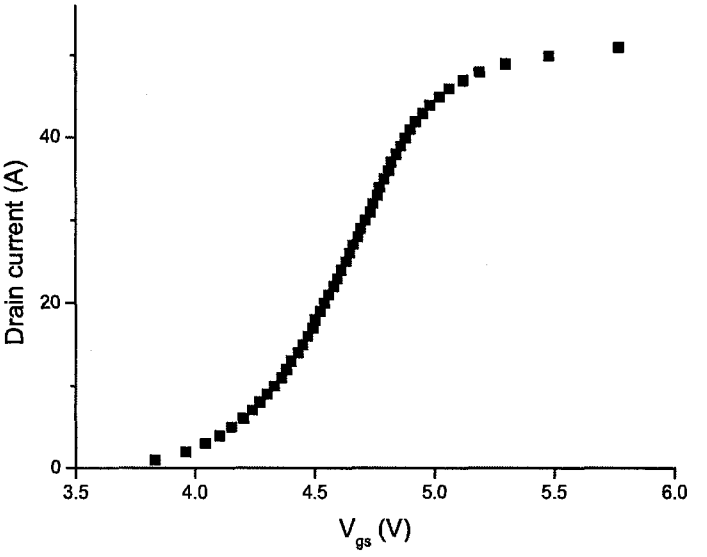

Figure A.3 Drain current vs V_{gs} for an IXFN180N20 MOSFET in series with a test load with the supply in constant voltage mode

saturation (the region where the curve levels off past 5.25 V) where the response is to low for good control to occur. If the supply is set in this regime the variation in current will be seen in the voltage drop across the shunt resistor in the switch box, and the supply voltage must be increased accordingly.

Appendix B
The Switch Box

In order to implement active control of the current and retain the ability to rapidly ($\leq 300\mu s$) switch the current as before required a redesign of the switch box which contains all of the FETs and the shunt resistor (the voltage drop across which is used to calibrated the field). Fig. B.1 shows the layout of the switch box.

All of the FETs (and especially the pair labelled F3) servo significant amounts of current and can dissipate significant amounts of heat. All FETs were tightly screwed down on to smooth water-cooled plates with heat sink compound covering the underside of the FETs to ensure good thermal contact between the plates and the FETs. The water flowing through the plates comes from the buildings chilled water supply. Pairs of FETs with similar control voltage vs current curves were used to cut the current individual FETs received and ensure the load was as evenly shared as possible. For FETs operated fully open or closed this simply cuts the power servoed by any individual device and helps prolong it's life. For the pair F3 (which receive the feedback from the control circuit), however, using similar devices is of particular importance - they servo far more power in the high field where they are operated in an intermediate regime where the resistance (and hence power dissipated) is far higher. In addition to providing some protection, pairing like FETs ensures the response to the feedback is similar for both devices, which helps reduce non-linearity in the response of the system.

Each pair of FETs (and the ESS supply itself) are protected with transient voltage suppressors (shown in Fig. B.1) purchased from MDE Semiconductor, Inc. These bi-directional devices cannot servo DC current, but instead are designed to take very brief large surges which can result from rapidly switching large currents as happens when the supplies are switched off rapidly with the FETs.

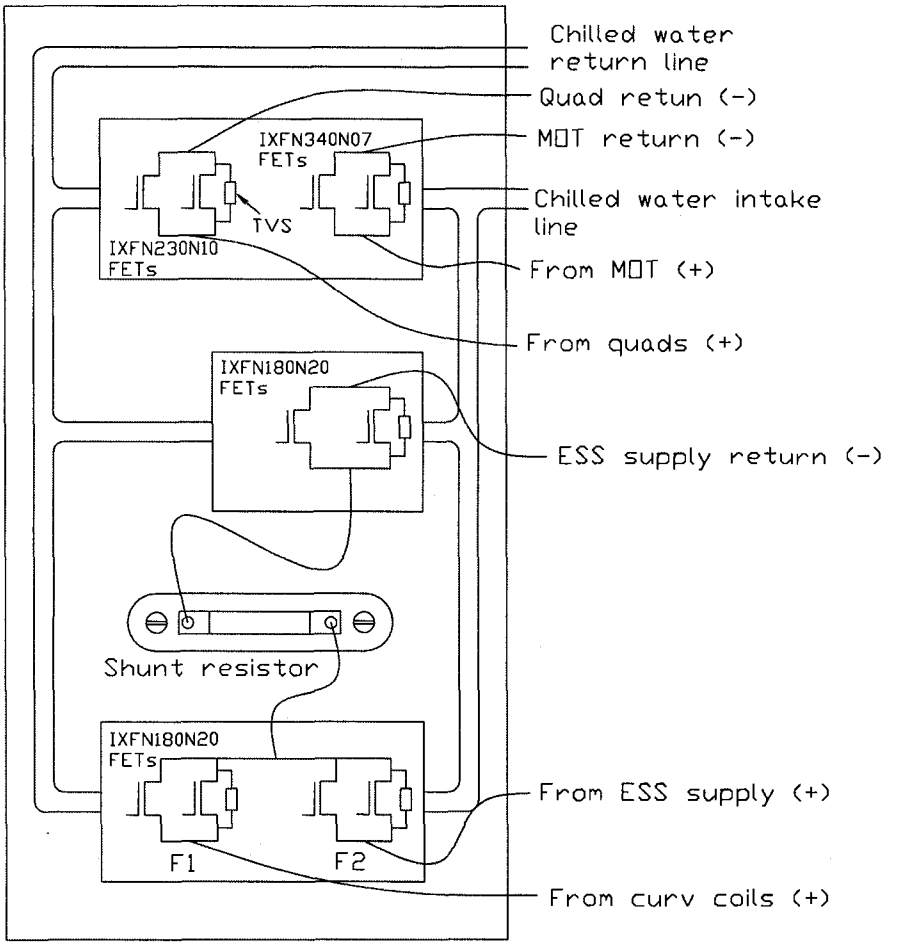

Figure B.1 The layout of the switch box showing component locations and connections.

The lid of the switch box mounts two 120 mm fans (one blowing air into the box, and the other pulling air out of the box) which provide cooling for the cabling and circulate air.

References

1. A. G. Truscott, K. E. Strecker, W. I. McAlexander, G. B. Partridge, and R. G. Hulet. "Observation of Fermi pressure in a gas of trapped atoms." *Science* **291** 2570–2572 (2001).

2. K. E. Strecker, G. P. Partridge, A. G. Truscott, and R. G. Hulet. "Formation and propagation of matter-wave soliton trains." *Nature* **417** 150–153 (2002).

3. K. E. Strecker, G. B. Partridge, and R. G. Hulet. "Conversion of an atomic Fermi gas to a long-lived molecular Bose gas." *Physical Review Letters* **91** 080406–1–4 (2003).

4. G. B. Partridge, W. Li, Y. A. Liao, R. G. Hulet, M. Haque, and H. T. C. Stoof. "Deformation of a trapped Fermi gas with unequal spin populations." *Physical Review Letters* **97** 190407–1–4 (2006).

5. M. J. Junker. *Photoassociation in a Quantum Degenerate Gas of ^7Li.* Masters, Rice University (2004).

6. C. E. Wieman and L. Hollberg. "Using diode lasers for atomic physics." *Rev. Sci. Instrum.* **62** 1–20 (1991).

7. J. Gaebler. *A High Powered Diode Laser System for a Lithium Magneto Optical Trap.* Undergraduate thesis, Rice University (2004).

8. K. E. Strecker. *Tunable Interaction in Quantum Degenerate Lithium.* Ph.D. thesis, Rice University (2004).

9. M. W. Fleming and A. Mooradian. "Spectral characteristics of external-cavity controlled semiconductor lasers." *IEEE J. Quant. Electron.* **17** 44–59 (1981).

10. C. A. Sackett. *Dynamics of Bose-Einstein condensation in ^7Li.* Ph.D. thesis, Rice University (1998).

11. M. Praeger, V. Vuletic, T. Fischer, T. W. Hansch, and C. Zimmermann. "A broad emitter diode laser system for lithium spectroscopy." *Applied Physics B* **67** 163–166 (1998).

12. G. Ferrari, M. O. Mewes, F. Schreck, and C. Salomon. "High-power multiple-frequency narrow-linewidth laser source based on a semiconductor tapered amplifier." *Opt. Letters* **24** 151–153 (1999).

13. K. G. Libbrecht and J. L. Hall. "A low-noise high-speed diode laser current controller." *Rev. Sci. Instruments* **64** 2133–2135 (1993).

14. B. Baysinger. *Semiconductor Laser System for Magneto-Optical Trapping of Fermionic ^6Li.* Undergraduate thesis, Rice University (2004).

15. M. O. Mewes, G. Ferrari, A. Sinatra, and C. Salomon. "Simultaneous magneto-optical trapping of two lithium isotopes." *Phys. Rev. A* **61** 011403–1–4 (1999).

16. W. I. McAlexander. *Low Energy Collisional Interactions in Magnetically Trapped Lithium.* Ph.D. thesis, Rice University (2000).

17. G. B. Partridge. *An Improved System for Creating Ultracold Fermi Gases of ^6Li.* Masters thesis, Rice University (2003).

18. J. M. Gerton. *Molecular spectroscopy of a Bose-Einstein condensate with attractive interactions.* Ph.D. thesis, Rice University (2001).

19. G. Ritt, G. Cennini, C. Geckeler, and M. Weitz. "Laser frequency offset locking using a side of filter technique." *Appl. Phys. B* **79** 363–365 (2004).

20. C. Ospelkaus. *Fermi-Bose mixtures - From mean field interactions to ultracold chemisty.* Ph.D. thesis, University of Hamburg (2006).

21. E. Tiesinga, B. J. Verhaar, and H. T. C. Stoof. "Threshold and resonance phenomena in ultracold ground-state collisions." *Phy. Rev. A* **47**(5) 41144122 (1993).

22. S. Inouye, M. R. Andrews, J. Stenger, H.-J. Miesner, D. M. Stamper-Kurn, and W. Ketterle. "Observation of Feshbach resonances in a Bose-Einstein condensate." *Nature* **392** 151 (1998).

23. R. A. Duine and H. T. C. Stoof. "Atom-molecule coherence in Bose gases." *Phys. Rep.* **396** 115–195 (2004).

24. M. Bartenstein *et al.* "Precise determination of ^{6}Li cold collision parameters by radio-frequency spectroscopy on weakly bound molecules." *Physical Review Letters* **94** 103201–1–4 (2005).

25. K. E. Strecker, G. B. Partridge, A. G. Truscott, and R. G. Hulet. "Bright matter wave solitons in Bose-Einstein condensates." *New J. Phys.* **5** 73.1–73.8 (2003).

26. L. Khaykovich, F. Schreck, G. Ferrari, T. Bourdel, J. Cubizolles, L. D. Carr, Y. Castin, and C. Salomon. "Formation of a matter-wave bright soliton." *Science* **296** 1290–1293 (2002).

27. I. D. Prodan, M. Pichler, M. Junker, R. G. Hulet, and J. L. Bohn. "Intensity dependence of photoassociation in a quantum degenerate atomic gas." *Physical Review Letters* **91** 080402–1–4 (2003).

28. G. B. Partridge, K. E. Strecker, R. I. Kamar, M. W. Jack, and R. G. Hulet. "Molecular probe of pairing in the bec-bcs crossover." *Physical Review Letters* **95** 020204–1–4 (2005).

29. Carl Blake and Chris Bull. *IGBT or MOSFET: Choose Wisely.* International Rectifier, http://www.irf.com/technical-info/whitepaper/choosewisely.pdf.

30. Paul Horowitz and Winfield Hill. *The Art of Electronics: Second Edition.* Cambridge, Cambridge (1989).

31. L. Sanchez-Palencia, D. Clément, P. Lugan, P. Bouyer, G. V. Shlyapnikov, and A. Aspect. "Anderson Localization of Expanding Bose-Einstein Condensates in Random Potentials." *Physical Review Letters* **98** 210401–1–4 (2006).

32. C. H. Schunck, M. W. Zwierlein, C. A. Stan, S. M. F. Raupach, and W. Ketterle. "Feshbach resonances in fermionic ^{6}Li." *Phys. Rev. A* **71** 045601–1–4 (2005).

33. J.K. Chin, D.E. Miller, Y. Liu, C. Stan, W. Setiawan, C. Sanner, K. Xu, and W. Ketterle. "Fermionic superfluidity in a lattice." *Nature* **443** 961–964 (2006).

34. C. Buttay. "Metaloxidesemiconductor structure." *Retrieved 06/10/07* http://en.wikipedia.org/wiki/Mosfet (2006).